



**HAL**  
open science

# THE ELECTRON CYCLOTRON MASER INSTABILITY

P. Sprangle, V. Granatstein, A. Drobot

► **To cite this version:**

P. Sprangle, V. Granatstein, A. Drobot. THE ELECTRON CYCLOTRON MASER INSTABILITY. Journal de Physique Colloques, 1977, 38 (C6), pp.C6-135-C6-152. 10.1051/jphyscol:1977613 . jpa-00217197

**HAL Id: jpa-00217197**

**<https://hal.science/jpa-00217197>**

Submitted on 4 Feb 2008

**HAL** is a multi-disciplinary open access archive for the deposit and dissemination of scientific research documents, whether they are published or not. The documents may come from teaching and research institutions in France or abroad, or from public or private research centers.

L'archive ouverte pluridisciplinaire **HAL**, est destinée au dépôt et à la diffusion de documents scientifiques de niveau recherche, publiés ou non, émanant des établissements d'enseignement et de recherche français ou étrangers, des laboratoires publics ou privés.

## THE ELECTRON CYCLOTRON MASER INSTABILITY (\*) (+)

P. SPRANGLE, V. L. GRANATSTEIN and A. DROBOT (\*\*)

Naval Research Laboratory Washington, D. C. 20375, U. S. A.

**Résumé.** — L'instabilité maser cyclotron a une double importance ; d'abord il y a un intérêt scientifique fondamental dans cette forte instabilité d'un ensemble d'électrons spiralant dans un champ magnétique ; ensuite, cette instabilité est à la base d'une nouvelle catégorie de générateurs d'ondes millimétriques de puissance (gyrotrons), qui sont en train de trouver une application au chauffage r. f. de plasma dans les appareils de recherche sur la fusion contrôlée. Dans cet article, les théories linéaire et non linéaire sont considérées. Des effets relativistes associés avec les électrons spiralant sont responsables de l'amplification d'un mode transverse électrique de guide d'onde. L'évolution temporelle non linéaire de l'amplitude du champ et de la fréquence d'une seule onde, est décrite. La dynamique d'onde non linéaire est déterminée de façon auto-consistante à partir des orbites non linéaires des particules, par les équations de force et d'onde. On trouve deux mécanismes de saturation de la croissance de l'onde : (1) épuisement de l'énergie libre disponible dans les électrons tournants ; (2) piégeage en phase des électrons avec l'onde. La compétition entre les deux mécanismes de saturation conduit à un étroit maximum pour l'efficacité de conversion d'énergie en fonction de l'énergie du faisceau. La théorie a été utilisée pour construire un amplificateur gyrotron non linéaire ayant 340 kW de puissance en sortie à 35 GHz avec une efficacité optimisée à 51 % dans le référentiel du plasma.

**Abstract.** — The cyclotron maser instability has a two-fold importance, first, there is fundamental scientific interest in this strong instability of an ensemble of spiralling electrons in a magnetic field ; second, this instability is the basis for a new class of powerful millimeter wave generators (gyrotrons) which are finding application to r.f. heating of plasma in controlled fusion research devices. In this paper, both the linear theory and the nonlinear theory of the instability are considered. Relativistic effects associated with the spiralling electrons are responsible for amplification of a transverse electric waveguide mode. The temporal nonlinear evolution of the field amplitude and frequency of a single wave is described. The nonlinear wave dynamics are selfconsistently determined from the nonlinear particle orbits through the force and wave equations. Two mechanisms for saturation of wave growth are found : (1) depletion of the available free energy associated with the rotating electrons ; (2) phase trapping of the electrons in the wave. Competition between the two saturation mechanisms leads to a peaking in the energy conversion efficiency as a function of beam energy. The theory has been used to design a nonlinear gyrotron amplifier with 340 kW output power at 35 GHz with efficiency optimized at 51 % in the laboratory frame.

**1. Introduction.** — The electron cyclotron maser instability is generated by a beam of electrons following helical trajectories around the lines of an axial magnetic field. The electron ensemble interacts unstably with an electromagnetic wave whose frequency is near the Doppler shifted electron cyclotron

frequency (or its harmonics). Initially, the phase of the electrons in their cyclotron orbits are random, but phase bunching can occur because of the relativistic dependence of electron cyclotron frequency on electron energy. Early descriptions of the physical process are to be found in the works of Twiss [1], Schneider [2], and Gapanov [3]. The first experimental observation was made in 1959 by Pantell [4] and a deliberate experimental study was made in 1964 by Hirshfield and Wachtel [5]. An extensive description of the early work is to be found in recent review papers [6].

From the above description it is clear that the cyclotron maser emits radiation at a wavelength determined by the strength of an applied magnetic field, and not by the dimensions of some resonant structure. Thus unlike most other microwave tubes, the internal dimensions of the device may be large compared to the wavelength, and high power handling

(\*) This manuscript is an updated version of the paper appearing in «The Linear and Self-Consistent Nonlinear Theory of the Electron Cyclotron Maser Instability » by P. Sprangle and A. T. Drobot, from the IEEE TRANSACTIONS on Microwave Theory and Techniques, June 1977, Vol. MTT-25, No. 6. Copyright © 1977 by The Institute of Electrical and Electronics Engineers, Inc.

(\*\*) A. Drobot is with Science Applications, Inc., McLean, Va.

(+) Work supported in part by the Naval Material Command, Task RF 34-372-401, by the Army Ballistic Missile Defense Advanced Technology Center, MIPR W31RPD-73-Z787, and by the Naval Surface Weapons Center (Dahlgren), Task SF32-302-41B.

capability becomes compatible with operation at millimeter and submillimeter wavelengths. Indeed, the highest recorded millimeter wave power, both peak and average have been achieved through the cyclotron maser process. The high peak powers were achieved in a series of experiments using intense relativistic electron beams ( $V \sim 1$  MV,  $I \sim 30$  kA) and powers achieved include 900 MW at  $\lambda = 4$  cm [7], 350 MW at  $\lambda = 2$  cm [8], 8 MW at  $\lambda = 8$  mm [9], and 2 MW at  $\lambda = 4$  mm [9]; however, efficiency of converting electron beam energy to e.m. radiation was only  $\sim 1\%$ . Our analysis shows that there are a number of reasons for the observed low efficiencies with intense relativistic electron beams, among them the high levels of current and voltage and excessive energy spread in the beam.

On the other hand, the high average powers were generated with high efficiency and with current and voltage levels similar to those in conventional microwave tubes; thus, the high average power work leads directly to practical devices which already are finding application in electron cyclotron resonance heating (ECRH) of Tokamak plasmas [10]. The initiative in developing high average power cyclotron masers has been taken by workers at the Gorkii State University (USSR) [11, 12] who have called their devices *gyrotrons*. The key to achieving efficient devices was careful design of a new type of electron gun. In the Gorkii studies, a crossed-field magnetron injection gun was used to launch an annular electron beam with a large fraction of energy transverse to the axis and with minimum energy spread. Work on nonuniform cross-section open resonators to optimize beam-wave coupling has also taken place. All together these developments have led to demonstration of a technological breakthrough in CW millimeter wave generation. Using a superconducting magnet, Zaytsev, *et al.* [11] have generated the following CW powers: 12 kW at  $\lambda = 2.78$  mm with

31 % efficiency; 2.4 kW at  $\lambda = 1.91$  mm with 9.5 % efficiency; and 1.5 kW at  $\lambda = 0.92$  mm with 6.2 % efficiency. Figure 1 compares these results with CW power available from other microwave devices; an advance in CW power capability by 4 orders of magnitude is clearly indicated.

Work on the linear theory of the cyclotron maser shows that the instability is due to the coupling of the supraluminous TE waveguide mode and a beam cyclotron mode [13-17]. The instability may be either absolute or convective in nature. For a review of the theory on excited nonlinear oscillators as applied to the cyclotron maser, see the article by Gapanov, *et al.* [18].

To our knowledge, the first nonlinear evaluation of the electron cyclotron maser mechanism involved numerical integration of the electron orbits in fields of either constant amplitude and/or constant frequency [14, 19-13]. These nonlinear theories do not fully treat the particles and wave dynamics in an inherently self-consistent manner.

In this paper a comprehensive study of the self-consistent nonlinear evolution of the electron cyclotron maser instability is presented. We have included both a time-dependent frequency shift and a time dependent field amplitude in our analysis. A rather simple physical picture of the nonlinear behavior of this instability shows that there are two mechanisms responsible for wave saturation [24]. The analysis is self-consistent in that the particle and wave dynamics are treated as a unit. Saturation efficiencies at the fundamental waveguide mode and cyclotron mode are obtained. A method of externally controlling the saturation process, and thereby further improving conversion efficiencies, is discussed.

The physical mechanism of the electron cyclotron maser is described in Section 2. Properties of the linear dispersion relation are discussed in Section 3. Here simple expressions for the linear growth rate and frequency shift are obtained. The linear theory indicates that the growth rate maximizes when the axial beam velocity is equal to the group velocity of the excited wave. This fact can be used to simplify the analysis by performing all calculations in the beam frame which now coincides with the cutoff frame where the axial number,  $k_0$ , vanishes. The results are then transformed back to the laboratory frame. In Section 4 we derive the equations for the nonlinear growth rate and frequency shift of the excited wave. The nonlinear single wave formalism treats both the particle and wave dynamics self consistently. The equivalence of our temporal model with the steady state spatial growth of a wave in an amplifier is pointed out. A number of simplifying assumptions have been made in our analysis, the one of major practical importance being neglect of initial beam temperature. The conditions for the validity of this approximation are discussed in Section 5. Section 6 describes the two nonlinear saturation

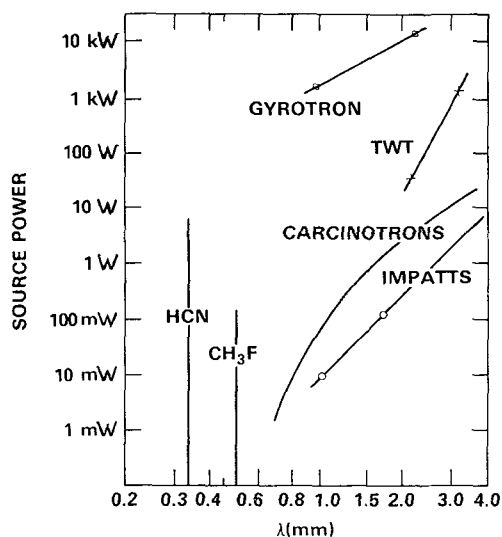


FIG. 1. — State-of-the-art CW power sources.

processes of the cyclotron maser instability. There we show that the depletion of free energy and/or particle phase trapping is responsible for wave saturation. The dominant mechanism depends on the initial choice of beam parameters. Simple analytic expressions for the field amplitude at saturation are obtained. From the slow time scale orbit equations we obtain a constant of the motion for a fixed amplitude and frequency field. This constant is used to examine the nonlinear particle orbits in phase space. Section 7 contains the numerical results of our formalism for a wide range of beam parameters. These results include field amplitudes and efficiencies at saturation. Comparison of these results with the analytic expressions given in Section 6 is made. Methods for improving the efficiency at saturation are also discussed and examples given. Section 8 describes application of the theory to designing an efficient millimeter wave gyrotron in the form of a travelling wave amplifier with output power of hundreds of kilowatts.

**2. Physical Mechanism.** — Insight into the physical mechanism responsible for the electron cyclotron maser instability can be obtained from the particle trajectories shown in figures 2a and 2b. These figures

show the orbit dynamics of sample electrons initially uniformly distributed along a gyro orbit. The electrons are rotating in the counter clockwise direction about a uniform and constant magnetic field,  $B_0 \hat{e}_z$ . Without loss of generality we assume the electron velocity in the  $z$  direction to be zero. The initial radius of the sample electron ring is the Larmor radius

$$r_{0L} = v_{0\perp} / (\Omega_0 / \gamma_{0\perp})$$

where  $v_{0\perp}$  is the initial perpendicular velocity,

$$\Omega_0 = |e| B_0 / m_0 c$$

is the nonrelativistic cyclotron frequency and

$$\gamma_{0\perp} = (1 - v_{0\perp}^2 / c^2)^{-1/2}$$

is the relativistic factor.

The introduction of a small constant amplitude electric field,

$$E_y(t) = \varepsilon_0 \cos(\omega_0 t) \hat{e}_y,$$

as shown in figure 2a, will alter the particle orbits. We first examine the particle trajectories when the frequency of the electric field is equal to the initial relativistic cyclotron frequency,  $\omega_0 = \Omega_0 / \gamma_{0\perp}$ . The time rate of change of the particle energy is

$$d\varepsilon_p / dt = - |e| v_y(t) E_y(t)$$

where  $v_y(t)$  is the  $y$  component of particle velocity. With the initial choice of field direction shown in figure 2a particles 8, 1 and 2 will lose energy and tend to spiral inward. The relativistic cyclotron frequency of these particles will increase, since  $\gamma_{\perp}$  decreases, and their phase will tend to slip ahead of the wave. Particles 4, 5 and 6, on the other hand, will gain energy, their cyclotron frequency will decrease and they will tend to spiral outward. The phase of these particles will tend to slip behind the wave. After an integral number of wave periods, the particles will become bunched around the positive  $y$ -axis. Particle bunching is, therefore, caused by relativistic effects, since the rotational frequency of the electrons is energy dependent.

To obtain a net exchange of energy between the particles and wave,  $\omega_0$  must be slightly greater than  $\Omega_0 / \gamma_{0\perp}$ . If  $\omega_0 \gtrsim \Omega_0 / \gamma_{0\perp}$ , the particles on the average traverse a coordinate space angle less than  $2\pi$  in a wave period,  $2\pi / \omega_0$ . All the particles will then slip behind the wave and the distribution of particles after an integral number of wave periods will be bunched in the upper half plane as shown in figure 2b. As a result of the phase slippage between the particles and the field, the net kinetic energy of the ensemble of particles decreases. Conservation of total energy implies that the field amplitude increases resulting in instability. If  $\omega_0$  remains greater than  $\Omega_0 / \gamma_{\perp}$ , the particles will continue to slip behind the wave.

Depending on the initial beam parameters, the group of bunched beam particles may: i) continue

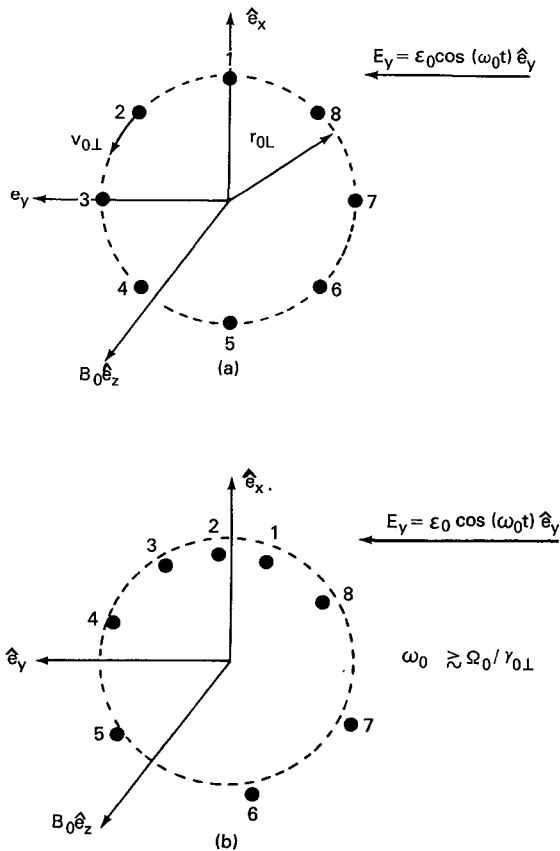


FIG. 2. — The mechanism responsible for the electron cyclotron maser illustrated by orbits of test particles in velocity space in the presence of a small external field. (a) initial particle and (b) bunched particles after several cycles.

to slip behind the wave, or ii) initially slip behind the wave, reverse itself and begin to oscillate about the positive  $y$ -axis. We will see later on that these two different processes lead to two distinct saturation mechanisms. In either case, the bunched particles will eventually appear in the lower half of the transverse plane after an integral number of wave periods. When this occurs, the particles will gain energy and the wave amplitude will begin to decrease.

**3. Linear Theory.** — Using the Maxwell-Vlasov equations, the linear dispersion relation for the electron cyclotron maser instability is easily calculated [10, 19]. The electron beam and waveguide configuration employed for this purpose is shown in figure 3. This configuration will also be used in the

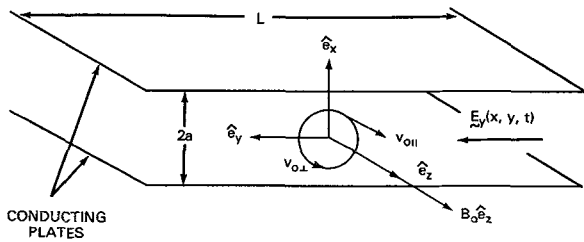


FIG. 3. — The electron cyclotron maser configuration in plane geometry.

nonlinear analysis. In figure 3 a beam of gyrating and drifting particles is assumed to have the same perpendicular velocity,  $v_{0\perp}$ , and parallel velocity,  $v_{0\parallel}$ , with respect to the applied axial magnetic field  $B_0$ . The guiding centers of the particles lie midway between the two conducting plates. The system of particles and fields is assumed independent of the spatial  $y$  variable. The field components within the waveguide are those of a  $TE_{on}$  mode (i. e.,  $E_y$ ,  $B_z$  and  $B_x$  are the only nonvanishing field components). The functional dependence of the fields on  $z$  and  $t$  has the form  $\exp(i(k_0 z - \omega t))$ . The perturbed current density when used in conjunction with the wave equation for  $E_y(x, z, t)$  leads to the following linear dispersion relation in the laboratory frame for the configuration shown in figure 3,

$$\omega^2 - c^2(k_0^2 + k_n^2) = \delta_{nl}(\omega_b^2/\gamma_0)$$

$$\left[ \frac{(\omega - k_0 v_{0\parallel}) Q_{nl}}{(\omega - k_0 v_{0\parallel} - l\Omega_0/\gamma_0)} - \frac{\beta_{0\perp}^2(\omega^2 - c^2 k_0^2) W_{nl}}{(\omega - k_0 v_{0\parallel} - l\Omega_0/\gamma_0)^2} \right] \quad (1)$$

where  $k_n = \pi n/2a$  is the perpendicular wave number,  $n = 1, 2, 3, \dots$  is the waveguide mode number,

$$\delta_{nl} = (1 + (-1)^{n+l}), \quad \omega_b^2 = 4\pi |e| \sigma_0/m_0 a$$

is the modified plasma frequency,  $\sigma_0$  is the surface charge density of the beam in the  $x-y$  plane,  $l = 1, 2, 3$  is the magnetic harmonic number,

$$\gamma_0 = (1 - v_{0\parallel}^2/c^2 - v_{0\perp}^2/c^2)^{-1/2},$$

$$\Omega_0 = |e| B_0/m_0 c, \quad \beta_{0\perp} = v_{0\perp}/c,$$

$$Q_{nl} = x_n(l^2/x_n^2 - 1) d(J_l(x_n))^2/dx,$$

$$W_{nl} = (dJ_l(x_n)/dx)^2,$$

$$x_n = \beta_{0\perp} c k_n / (\Omega_0/\gamma_0)$$

and  $J_l$  is the Bessel function of order  $l$ . If  $n+l$  is odd, the  $TE_{on}$  mode is stable since the right hand side of eq. (1) vanishes [25]. The first term in the bracket on the right hand side of (1) is always stabilizing while the second term is always destabilizing. Furthermore, the frequency of the unstable wave in the rest frame of the electrons is slightly greater than the cyclotron frequency,  $\gamma_0(\omega - k_0 v_{0\parallel}) \gtrsim \Omega_0$ . We have seen in Section 2 that this requirement is necessary for a phase slippage to occur between the particles and field. It is clear from the dispersion relationship in Eq. (1) that the maximum growth rate of the modified  $TE_{on}$  mode occurs for frequencies and wave numbers near the intersection of the vacuum waveguide mode

$$\omega^2 - c^2(k_0^2 + k_n^2) = 0,$$

and the cyclotron mode,  $\omega - k_0 v_{0\parallel} - l\Omega_0/\gamma_0 = 0$ . When the perpendicular velocity of the particles,  $v_{0\perp}$ , vanishes the cyclotron wave is a positive energy wave. Since the waveguide mode is also a positive energy wave, there can be no instability for  $v_{0\perp} = 0$ . If, however,  $v_{0\perp} \neq 0$ , the cyclotron mode splits into a positive and negative energy polarity wave as can be seen from the fact that  $(\omega - k_0 v_{0\parallel} - l\Omega_0/\gamma_0)^2$  appears in the denominator of the destabilizing term of eq. (1). The coupling of the negative energy cyclotron wave and positive energy waveguide mode is responsible for the instability. In the limit of vanishing beam density,  $\omega_b \rightarrow 0$ , or vanishing perpendicular velocity,  $v_{0\perp} \rightarrow 0$ , the opposite energy polarity cyclotron waves coalesce and become degenerate.

Seeking a solution to eq. (1) near the intersection of the modes we set  $\omega = \omega_0 + \delta\omega_0$  where

$$|\delta\omega_0| \ll \omega_0$$

and

$$\omega_0 = c(k_0^2 + k_n^2)^{1/2} = k_0 v_{0\parallel} + l\Omega_0/\gamma_0.$$

Substituting  $\omega = \omega_0 + \delta\omega_0$  into (1) and keeping terms to order  $(\delta\omega_0)^3$  yields the following relation

$$\delta^3\omega_0 - 3\Delta^2\omega_0\delta\omega_0 + 3Z_{nl}\Delta^2\omega_0 = 0 \quad (2)$$

where

$$\Delta\omega_0 = (l\Omega_0/\gamma_0(\delta_{nl}\omega_b^2/(6\gamma_0\omega_0))Q_{nl})^{1/2}$$

and

$$Z_{nl} = (x_n/l)^2 (W_{nl}/Q_{nl}) (l\Omega_0/\gamma_0).$$

The solutions of eq. (2) yield complex roots when  $Z_{nl} > (2/3) \Delta\omega_0$ . This condition can be stated as a threshold condition for instability, requiring that the perpendicular velocity be greater than a critical value [27],

$$\beta_{0\perp} > \beta_{\perp, \text{crit}}$$

where

$$\beta_{\perp, \text{crit}} = l(\Omega_0/\gamma_0) (Q_{nl}/W_{nl})^{1/2} \times [(2/27) \delta_{nl} \omega_b^2 Q_{nl}/(\gamma_0 \omega_0 l \Omega_0/\gamma_0)]^{1/4} / ck_n.$$

At the critical value of  $\beta_{\perp}$  the stabilizing and destabilizing terms in eq. (1) just balance each other. The beam has no free energy available for driving the instability when  $\gamma_{0\perp} = \gamma_{\perp, \text{crit}}$  where

$$\gamma_{\perp, \text{crit}} = (1 - \beta_{\perp, \text{crit}}^2)^{-1/2}.$$

The roots of eq. (2) can be easily evaluated in two regimes: (i)  $\beta_{0\perp} \gtrsim \beta_{\perp, \text{crit}}$ , and (ii)  $\beta_{0\perp} \gg \beta_{\perp, \text{crit}}$ . In the first regime, (i), the perpendicular energy of the beam is close to the critical value and the saturation is caused by the depletion of free energy. In the second regime, (ii), the perpendicular energy of the beam is well above the critical value and, as we will show in Section 6, the saturation mechanism for the instability is phase trapping of the particles by the excited wave.

*Case (i).* — Here,  $\beta_{0\perp} \gtrsim \beta_{\perp, \text{crit}}$  and the second term on the right hand side of eq. (1) is larger but comparable to the first term. The linear frequency shift and growth rate take the form:

$$\Delta\omega_i = \text{Re}(\delta\omega_0)_i = ((3/2) Z_{nl} \Delta^2 \omega_0)^{1/3} \approx \Delta\omega_0, \quad (3a)$$

$$\Gamma_i = \text{Im}(\delta\omega_0)_i = 3^{-1/2} (\Delta\omega_0)^{2/3} (3 Z_{nl}/2)^{-2/3} \times ((3 Z_{nl}/2)^2 - \Delta^2 \omega_0)^{1/2} \approx (Z_{nl} \Delta\omega_0 - 2 \Delta^2 \omega_0/3)^{1/2}. \quad (3b)$$

The growth rate for this case is proportional to the fourth root of the surface charge density.

*Case (ii).* Here,  $\beta_{0\perp} \gg \beta_{\perp, \text{crit}}$  and the second term on the righthand side of eq. (2) dominates. The linear frequency shift and growth rate of the wave are:

$$\Delta\omega_{ii} = \text{Re}(\delta\omega_0)_{ii} = (1/2) (3 Z_{nl} \Delta^2 \omega_0)^{1/3}, \quad (4a)$$

$$\Gamma_{ii} = \text{Im}(\delta\omega_0)_{ii} = 3^{1/2}/2 (3 Z_{nl} \Delta^2 \omega_0)^{1/3}. \quad (4b)$$

The growth rate for this case is proportional to the third root of the surface charge density,  $\sigma_0$ .

Choosing the practical situation where  $n = 1$ ,  $x_n$  is small,  $W_{11} \approx 1/4$ ,  $Q_{11} \approx 1/2$  and

$$\omega_0 \approx \Omega_0/\gamma_0 \approx ck_1$$

gives for the growth rates in cases i) and ii) the following

$$\Gamma_i = (1/3) (3(\beta_{0\perp}^2/r) \omega_0 \omega_b/\gamma_0^{1/2} - \omega_b^2/\gamma_0)^{1/2} \quad (5a)$$

and

$$\Gamma_{ii} \approx (2\sqrt{3})^{-1} (\beta_{0\perp} \omega_0 (\omega_b^2/4 \gamma_0))^{1/3}. \quad (5b)$$

The critical perpendicular velocity in this regime is given by

$$\beta_{\perp, \text{crit}} = \sqrt{2/3} (6(\omega_b^2/\gamma_0)/\omega_0^2)^{1/4}. \quad (6)$$

The condition that the  $n$ -th waveguide mode and the  $l$ -th synchronous mode intersect on the dispersion curve limits the value of  $x_n$ . It is easy to show that  $x_n$  is bounded by  $0 \leq x_n l$ . Figure 4 depicts the functions  $W_{nl}$  and  $Q_{nl}$  as functions of  $x_n$  for  $l = 1, 2, 3$  and 4. Figure 5 shows the dispersion diagram for the cyclotron maser instability when

$$v_{0\parallel} = 0, \omega_0 = ck_n = l\Omega_0/\gamma_0 \quad \text{and} \quad l = n = 1.$$

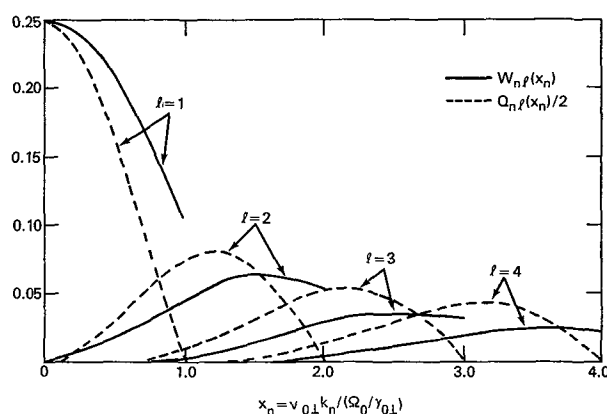


FIG. 4. — The functions  $Q_{nl}(x_n)$  and  $W_{nl}(x_n)$  vs.  $x_n$  for  $l = 1, 2, 3, 4$ .

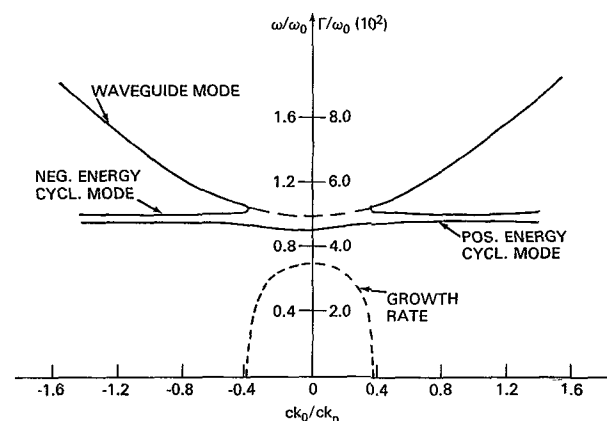


FIG. 5. — Typical dispersion curve for cyclotron maser instability. This case is for  $\gamma_{0\perp} = 1.2$ ,  $\omega_b/\sqrt{\gamma_{0\perp}} = 0.05 \omega_0$ ,  $\omega_0 = ck_n = l\Omega_0/\gamma_{0\perp}$  and  $l = n = 1$

Note that the cyclotron mode splits into two branches of negative and positive energy polarity. The negative energy cyclotron mode couples to the positive energy TE guide mode resulting in an instability. The growth

rate maximizes at  $k_0 = 0$ . If the cyclotron frequency were greater than the guide cut-off frequency,

$$\Omega_0/\gamma_{0\perp} > ck_n,$$

the growth rate would have two peaks at  $|k_0| > 0$ , symmetric about the  $k_0 = 0$  axis. The maximum growth rate for  $\Omega_0/\gamma_{0\perp} > ck_n$  is always less than the maximum growth rate for  $\Omega_0/\gamma_{0\perp} = ck_n$ . This can be seen in figure 6 where growth rate contours are shown as functions of  $(\Omega_0/\gamma_{0\perp})/(ck_n)$  and  $(ck_0/ck_n)$ .

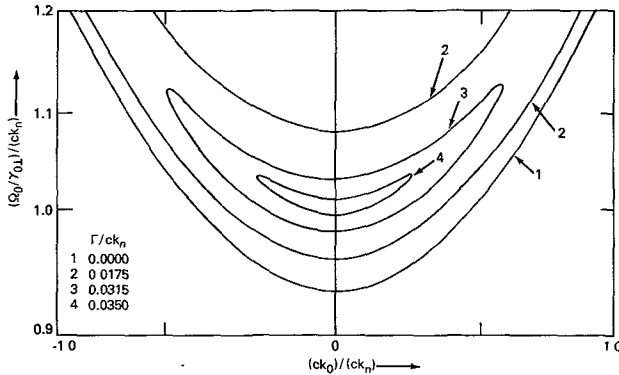


FIG. 6. — Contours of the growth rate for the cyclotron maser instability vs the parallel wave number and the cyclotron frequency. This case is for  $\gamma_{0\perp} = 1.2$  and  $\omega_b/\sqrt{\gamma_{0\perp}} = 0.05 \omega_0$ , where  $\omega_0 = ck_n$  and  $l = n = 1$ .

We note that, in general, the growth rate is maximum when the wave group velocity,  $v_g$ , equals the axial beam velocity,  $v_{0\parallel}$ . This becomes apparent if we transform to the beam frame ( $v_{0\parallel} = 0$ ) and note that for fixed  $\beta_{0\perp}$  and  $k_n$ , the growth rate is largest when  $k_0 = 0$  (i. e., when  $\omega_0 = \Omega_0/\gamma_0 = ck_n$ ). At  $k_0 = 0$ , the group velocity vanishes and, therefore,  $v_g = v_{0\parallel} = 0$  in this frame. Since both  $v_g$  and  $v_{0\parallel}$  transform in the same way, the growth rate maximizes when  $v_g = v_{0\parallel}$  in all frames.

**4. Non linear Formalism.** — In this section the basic equations governing the nonlinear behavior of the electron cyclotron maser instability are derived using a single wave model. The single wave approach

has been shown to be valid under a wide range of situations [24].

We first express the nonlinear dynamics of a single wave in terms of an ensemble average of the nonlinear particle orbits. The particle orbits are related to the fields through the relativistic Lorentz force equations. The resulting wave and force equations are then numerically solved to obtain the self-consistent behavior of the particles and the field. This analysis describes the nonlinear evolution of the field amplitude and frequency as a function of time. The beam and waveguide configuration shown in figure 3 is chosen as our basic model.

We have noted in Section 3 that the linear growth rate for the excited  $TE_{on}$  mode maximizes when the axial beam velocity and the wave group velocity are equal. We chose to analyze this situation since we are interested in the regime of maximum wave growth. Furthermore, for convenience, we transform to a frame in which both the axial beam velocity and wave group velocity vanish. Since the group velocity is now zero in this frame (cutoff frame), we note that the axial wave number of the wave is also zero. The electric field, in the cutoff frame, of the vacuum waveguide mode has the form

$$E_y(x, t) = -E_0(t) \cos(\omega_0 t + \alpha(t)) \sin(k_n(x - a)), \quad (7)$$

where  $k_n = \pi n/(2a)$  and  $n$  is a positive integer such that  $E_y(x, t)$  satisfies the appropriate boundary conditions at  $x = \pm a$ . In eq. (7) the frequency  $\omega_0$  is a constant, while the amplitude,  $E_0(t)$ , and the frequency shift,  $\partial\alpha(t)/\partial t$ , are weak functions of time (e. g.,  $\partial \ln(E_0(t))/\partial t$ ,  $\partial\alpha(t)/\partial t \ll \omega_0$ ). The amplitude  $E_0(t)$  can be expressed as

$$E_0(t) = \varepsilon_0 \exp \int_0^t \Gamma(t') dt', \quad (7)$$

where  $\varepsilon_0$  is the initial field amplitude and  $\Gamma(t)$  is the time dependent growth rate. We note that in the linear regime of the instability the frequency shift and growth rate are constant and equal to their linear values,  $\partial\alpha(t)/\partial t = \Delta\omega_L$  and  $\Gamma(t) = \Gamma_L$ .

Associated with the electric field in eq. (7) is the vector potential  $A_y(x, t)$  given by

$$A_y(x, t) = (c/\omega_0) \{ (1 - \dot{\alpha}/\omega_0) E_0 \sin(\omega_0 t + \alpha) + (\dot{E}_0/\omega_0) \cos(\omega_0 t + \alpha) \} \sin(k_n(x - a)), \quad (8)$$

where  $A_y(x, t)$  is valid to first order in the small parameters  $\Gamma(t)/\omega_0$  and  $\dot{\alpha}(t)/\omega_0$ . The time evolution of  $E_0(t)$  and  $\alpha(t)$  is determined by the particle current density,  $J_y(x, t)$ , through the wave equation for  $A_y(x, t)$ :

$$(\delta^2/\delta x^2 - c^{-2} \delta^2/\delta t^2) A_y = -4 \pi c^{-1} J_y. \quad (9)$$

Substituting (8) into the wave equation and keeping only lowest order terms in the small parameters  $\Gamma/\omega_0$  and  $\dot{\alpha}/\omega_0$  yields the relation:

$$\{ (\omega_0^2 - c^2 k_n^2 + (c^2 k_n^2 + \omega_0^2) (\dot{\alpha}/\omega_0) \} E_0 \sin(\omega_0 t + \alpha) - (c^2 k_n^2 + \omega_0^2) (\dot{E}_0/\omega_0) \cos(\omega_0 t + \alpha) \} \times \sin(k_n(x - a)) = -4 \pi \omega_0 J_y(x, t). \quad (10)$$

The current density for a discrete set of particles is given by :

$$J_y(x, t) = - \frac{|e| \sigma_0}{N} \sum_{i=1}^N v_y(\varphi_i, t) \delta(x - x(\varphi_i, t)), \quad (11)$$

where  $\sigma_0$  is the surface number density in the  $y - z$  plane,  $N$  is the number of particles on a gyro radius,  $\varphi_i$  is the initial velocity space angle of the  $i$ -th particle measured with respect to the  $x$  axis and  $x(\varphi_i, t)$ , is the  $x$  position on the  $i$ -th particle. In the limit as  $N \rightarrow \infty$ ,

$$N^{-1} \sum \rightarrow (2\pi)^{-1} \int_0^{2\pi} d\varphi_0$$

where  $\varphi_0$  replaces  $\varphi_i$ . In eq. (9) the velocity component  $v_y$  of the  $i$ -th particle is a function of only  $(\varphi_i, t)$  since we assume an initially cold particle distribution in velocity. Our theory can include an initially thermal particle distribution, which would add an average over the initial velocities in (11). We will show later in eq. (19) that for an initial energy spread,  $\delta\gamma_{\perp} \ll 2\gamma_{0\perp} \Delta\omega/(\Omega_0/\gamma_{0\perp})$ , the particle distribution can be considered monoenergetic at  $t = 0$ . The present analysis is valid when the inequality in eq. (25) is satisfied. This does not, however, prevent the particles from thermalizing as the instability develops. The wave equation can be separated into equations for  $E_0(t)$  and  $\alpha(t)$ . By multiplying eq. (10) by  $\sin(k_n(x - a))$ , integrating across the waveguide from  $x = -a$  to  $x = a$  and operating on the resulting equation with

$$\int_t^{t+2\pi/(\omega_0+\dot{\alpha})} dt' \begin{Bmatrix} \sin(\omega_0 t' + \alpha(t')) \\ \cos(\omega_0 t' + \alpha(t')) \end{Bmatrix},$$

we arrive at the following expressions, which are valid to order  $\Gamma/\omega_0, \dot{\alpha}/\omega_0$  :

$$\begin{aligned} \dot{\alpha}(t) = & \frac{\omega_0}{(\omega_0^2 + c^2 k_n^2)} \left[ c^2 k_n^2 - \omega_0^2 + \left\{ \frac{2|e|\sigma_0}{a} \omega_0(\omega_0 + \dot{\alpha}) \times \right. \right. \\ & \times \int_t^{t+2\pi/(\omega_0+\dot{\alpha})} dt' < v_y(\varphi_0, t') \sin(k_n(x(\varphi_0, t') - a)) \sin(\omega_0 t' + \alpha(t')) > \left. \left. \right\} \right. \\ & \times \left. \left\{ \int_t^{t+2\pi/(\omega_0+\dot{\alpha})} E(t') \sin^2(\omega_0 t' + \alpha(t')) dt' \right\}^{-1} \right], \quad (12) \end{aligned}$$

$$\begin{aligned} \Gamma(t) = & \frac{\omega_0}{\omega_0^2 + c^2 k_n^2} \left\{ \frac{2|e|\sigma_0}{a} \omega_0(\omega_0 + \dot{\alpha}) \int_t^{t+2\pi/(\omega_0+\dot{\alpha})} dt' < v_y(\varphi_0, t') \times \right. \\ & \times \sin(k_n(x(\varphi_0, t') - a)) \cos(\omega_0 t' + \alpha(t')) > \left. \right\} \\ & \times \left\{ \int_t^{t+2\pi/(\omega_0+\dot{\alpha})} E(t') \cos^2(\omega_0 t' + \alpha(t')) dt' \right\}^{-1}. \quad (12') \end{aligned}$$

in the above equations,

$$< \quad > = (2\pi)^{-1} \int_0^{2\pi} d\varphi_0$$

is the ensemble average over the initial particle phase. We note that the temporal averages in eqs. (12) and (12') are performed over the actual wave period,  $2\pi/(\omega_0 + \dot{\alpha})$ . Eq. (12) and (12') describe the linear as well as non-linear evolution of the wave frequency and amplitude in terms of the particle orbits. The only restriction placed on  $\Gamma(t)$  and  $\alpha(t)$  is that they vary little in a wave period,  $2\pi/(\omega_0 + \dot{\alpha})$ .

The righthand side of eqs. (12) and (12') contain the details of the particle dynamics which are related to the fields through the relativistic orbit equations. Defining  $\beta = \beta_x + i\beta_y$  where  $\beta_x = v_x/c$  and  $\beta_y = v_y/c$ , the relativistic orbit equation can be put into the form :

$$d\beta/dt = \frac{i\Omega_0}{\gamma_{\perp}} \beta + \frac{i|e|B_z(x, t)}{\gamma_{\perp} m_0 c} \beta - \frac{i|e|}{\gamma_{\perp} m_0 c} (1 - \beta(\beta - \beta^*)/2) E_y(x, t) \quad (13)$$

where  $\gamma_{\perp} = (1 - \beta\beta^*)^{-1/2}$ ,  $E_y(x, t) = -c^{-1} \partial A_y/\partial t$ ,  $B_z(x, t) = \partial A_y/\partial x$  and  $x$  is given by  $dx/dt = c(\beta + \beta^*)/2$ .

We now choose the solution for eq. (13) to be of the form :

$$\beta(\varphi_0, t) = \beta_{\perp}(\varphi_0, t) \exp(i\varphi(\varphi_0, t)), \quad (14)$$

where

$$\beta_{\perp}(\varphi_0, t) = (\beta_x^2 + \beta_y^2)^{1/2} = (\beta\beta^*)^{1/2}$$

and

$$\varphi(\varphi_0, t) = \int_0^t \psi(\varphi_0, t') dt' + \varphi_0 = \tan^{-1}(\beta_y/\beta_x)$$

is the velocity space angle at time  $t$ . Substituting eq. (14) into (13) and equating real and imaginary parts, we obtain the following fully relativistic equations for the velocity magnitude and velocity space angle

$$\frac{d\beta_{\perp}}{dt} = \frac{-|e| E_y(x, t)}{\gamma_{\perp}^3 m_0 c} \sin \varphi(\varphi_0, t), \quad (15)$$

$$\frac{d\varphi}{dt} = \frac{\Omega_0}{\gamma_{\perp}} - \frac{|e| E_y(x, t)}{\gamma_{\perp} m_0 c \beta_{\perp}} \cos \varphi(\varphi_0, t), \\ + \frac{|e| B_z(x, t)}{\gamma_{\perp} m_0 c} \quad (15)$$

where  $\gamma_{\perp} = (1 - \beta_{\perp}^2)^{-1/2}$  and  $dx/dt = c\beta_{\perp} \cos \varphi(\varphi_0, t)$ . Eq. (7), (12) and (15) form a set of coupled nonlinear equations which describe the evolution of the electron cyclotron maser instability in the single wave model.

In Appendix A we show that the results from linear theory can be recovered from these equations. The orbit equation in (13) when written on the slow time scale yields a constant of the motion which is discussed in Section 6. The constant is useful in forming a qualitative picture of the trapping and saturation process.

The amplitude of the electric  $E_0(t)$  can be related to average decrease in particle energy through the energy conservation equation. Conservation of total energy within the waveguide implies that :

$$\frac{1}{2a} \int_{-a}^a (\varepsilon_f(x, t) + \varepsilon_p(x, t)) dx = \varepsilon_t, \quad (16)$$

where

$$\varepsilon_f(x, t) = (E_y^2(x, t) + B_z^2(x, t))/8\pi$$

is the field energy density,

$$\varepsilon_p(x, t) = \sigma_0 < (\gamma(\varphi_0, t) - 1) \delta(x - x(\varphi_0, t)) > m_0 c^2$$

is the particle energy density and

$$\varepsilon_t = (\sigma_0/2a) (\gamma_0 - 1) m_0 c^2$$

is the average total energy density of the system. Substituting  $E_y = -c^{-1} \partial A_y / \partial t$  and  $B_z = \partial A_y / \partial x$  into (16) where  $A_y$  is given by eq. (8), and performing the spatial average as well as a temporal average, leads to the following expression for  $E_0(t)$  :

$$E_0(t) = \frac{2 m_0 c}{|e|} \omega_b \left( 1 + \left( \frac{ck_n}{\omega_0} \right)^2 (1 - 2 \dot{\alpha}/\omega_0) \right)^{-1/2} \times \\ \times (\gamma_{0\perp} - < \gamma_{\perp}(\varphi_0, t) >)^{1/2}, \quad (17)$$

where  $\omega_b = 4\pi |e|^2 \sigma_0 / (m_0 a)$  is a modified plasma frequency and  $\gamma_{0\perp}$  is the initial gamma of the particles. In deriving eq. (17), terms of order higher than  $\Gamma/\omega_0$  and  $\dot{\alpha}/\omega_0$  have been neglected. Since  $ck_n/\omega_0 \approx 1$  and  $\dot{\alpha}/\omega_0 \ll 1$ , the expression for  $E_0(t)$  can be simplified to :

$$E_0(t) \approx \frac{\sqrt{8} m_0 c}{|e|} \omega_b (\gamma_{0\perp} - < \gamma_{\perp}(\varphi_0, t) >)^{1/2}. \quad (18)$$

A simple analytic expression for  $< \gamma_{\perp}(\varphi_0, t) >$  at saturation which will permit us to determine the maximum field strength through eq. (18), is derived in Section 6.

Since our system of fields and particles is independent of the spatial variable  $y$ , we note that the  $y$  component of canonical momentum

$$P_y = \gamma_{\perp} m_0 v_y - c^{-1} |e| A_y(x, t) - \Omega_0 m_0 x$$

is a constant of the motion for each particle. The conservation of total energy as well as the  $y$  component of canonical angular momentum is monitored throughout the numerical simulations of eqs. (12) and (15) to ensure consistency.

The nonlinear model developed in this section is directly applicable to the experimental situation in which a wave is spatially amplified in the streaming direction of a gyrating beam. The saturation levels obtained with the present model are directly related to the saturation levels in an amplifier when the axial beam velocity equals the wave group velocity. As pointed out in Section 3, this situation corresponds to a grazing intersection of the waveguide mode with the beam cyclotron mode when viewed on the dispersion diagram. Furthermore, such a grazing intersection leads to an absolute maximum in the temporal growth rate. In a steady state amplifier the input wave amplitude initially grows exponentially, enters the nonlinear regime and saturates. If we follow a group of particles contained in a thin cross-sectional slab of the beam, we note that the net flow of total energy flux into this slab is zero since we only consider the case where the axial beam velocity and wave group velocity are equal. Therefore, in the reference frame of the particles, the field amplitude evolves in time. This is precisely the situation described by our model. With the appropriate Lorentz transformations the saturation levels of the spatially amplified wave can be obtained with the present temporal model.

**5. Temperature Consideration.** — In this paper we have considered the beam to be initially monoenergetic in the beam frame. The range of validity of this assumption requires some examination. Since refe-

rence will be made to quantities in both the laboratory and beam frames, we shall denote the former with unprimed variables and the latter with primes. It is clear that the cold beam approximation will be valid if the total initial spread in  $\gamma'_{\perp}$  satisfies

$$\delta\gamma'_{\perp} \ll 2(\gamma'_{0\perp} - \langle \gamma'_{\perp} \rangle),$$

where  $\langle \gamma'_{\perp} \rangle_s$  is the average value of gamma at saturation. In terms of efficiency, this condition becomes

$$\delta\gamma'_{\perp}/\gamma'_{0\perp} \ll 2\eta'(\gamma'_{0\perp} - 1)/\gamma'_{0\perp}, \quad (19)$$

where  $\eta'$  is the beam frame efficiency defined as

$$\eta' = (\gamma'_{0\perp} - \langle \gamma'_{\perp} \rangle_s)/(\gamma_{0\perp} - 1).$$

Since the unstable wave has an infinite parallel wavelength, in the beam frame, any spread in  $v'_{\parallel}$  is unimportant. Before considering the limitations on the thermal spread in  $v'_{0\perp}$  we will need the transformation rule for efficiency from the beam frame to the laboratory frame. Consider the relativistic Lorentz transformation of total field energy in the beam frame to the laboratory frame. Since the field momentum in the beam frame is zero, we have :

$$W_f = \gamma_{0\parallel} W'_f = \gamma_{0\parallel} \eta' W'_b, \quad (20)$$

where  $W_f$  and  $W_b$  are the total field and particle energy in the laboratory frame. The power in the electromagnetic field can be written as :

$$P_f = v_{0\parallel} W_f/\Delta z = v_{0\parallel} \eta' W'_b/\Delta z, \quad (21)$$

where  $\Delta z$  is the axial extent of the volume element which contains the total field energy  $W_f$ . The total beam energy,  $W'_b$ , in the beam frame can be written as :

$$W'_b = \eta'_b(\gamma'_{0\perp} - 1) m_0 c^2 A \Delta z', \quad (22)$$

where  $A = 2r_L L$  is the cross sectional area of the beam and  $\Delta z'$  is the axial extent of the volume element in the beam frame. Substituting eq. (22) into (21) and using the relationships

$$\eta'_b \Delta z' = \eta_b \Delta z \quad \text{and} \quad \gamma_{0\parallel} = \gamma_0/\gamma'_{0\perp}$$

yields the result :

$$P_f = \frac{\gamma_0(\gamma'_{0\perp} - 1)}{\gamma'_{0\perp}(\gamma_0 - 1)} \eta' P_b.$$

The transformation rule for efficiency is therefore

$$\eta = \frac{\gamma_0(\gamma'_{0\perp} - 1)}{\gamma'_{0\perp}(\gamma_0 - 1)} \eta' \quad (23)$$

where  $\eta$  is the efficiency in the laboratory frame.

To define the beam qualities necessary for the validity of our cold beam approximation, it is useful to express eq. (19) in terms of laboratory frame quantities. The righthand side of eq. (19) can be

written in terms of laboratory frame quantities by using the transformation rule for efficiency. Using the results of eq. (23), the inequality in eq. (26) becomes

$$\delta\gamma'_{\perp}/\gamma'_{0\perp} \ll \frac{2(\gamma_0 - 1)}{\gamma_0} \eta, \quad (24)$$

where

$$\gamma_0 = (1 - v_{0\parallel}^2/c^2 - v_{0\perp}^2/c^2)^{-1/2}.$$

A spread in the beam frame gamma,  $\delta\gamma'_{\perp}$ , can arise from (a) a finite beam temperature in the laboratory frame or, in the case of a monoenergetic beam in the laboratory frame, (b) a spread in the velocity space angle of the particles.

In case (a) only a temperature spread in the perpendicular velocity is considered, so that

$$v_{\perp} = v_{0\perp} + \gamma v_{\perp}$$

where  $\Delta v_{\perp}$  is the thermal component of velocity. Only perpendicular temperature is considered since a parallel temperature in the laboratory frame,  $\Delta v_{\parallel}$ , contributes a higher order correction to  $\delta\gamma'_{\perp}$  than  $\Delta v_{\perp}$  if  $\Delta v_{\parallel}$  and  $\Delta v_{\perp}$  are of the same order. Since the perpendicular momentum is frame invariant,  $\gamma v_{\perp} = \gamma'_{\perp} v'_{\perp}$ , we find that the thermal spread in  $\gamma$  takes the form :

$$\Delta\gamma = \pm \gamma_{0\parallel} \Delta\gamma'_{\perp}, \quad (25)$$

where

$$\gamma_{0\parallel} = (1 - v_{0\parallel}^2/c^2)^{-1/2},$$

$v_{0\parallel}$  is the axial laboratory frame velocity and

$$\Delta\gamma'_{\perp} = 2(v_{0\perp}/c) \gamma_0^3 \Delta v_{\perp}/c$$

is the thermal spread in  $\gamma'_{\perp}$  due to

$$\Delta v'_{\perp} = \gamma_{0\parallel} \Delta v_{\perp}.$$

Substituting eq. (25) into (24) gives the following requirement for neglecting thermal effects in  $v_{\perp}$  :

$$\Delta\gamma/(\gamma_0 - 1) \ll 2\eta. \quad (26)$$

In the above inequality the efficiency,  $\eta$ , is calculated using the cold beam approximation.

In case (b) the particles have the same energy, however, a spread in the velocity components exists. Consequently, the particle velocity components in the laboratory frame can be written as

$$v_{\perp} = v_{0\perp} - v_{0\parallel} \Delta\theta \quad (27a)$$

$$v_{\parallel} = v_{0\parallel} + v_{0\perp} \Delta\theta, \quad (27b)$$

where  $|\Delta\theta| \ll 1$  is the spread of the velocity space angle, i. e., the angle between the total velocity vectors of the particles. To first order in  $\Delta\theta$ , we see that

$$v_{\parallel}^2 + v_{\perp}^2 = v_{0\parallel}^2 + v_{0\perp}^2,$$

so that the system of particles is monoenergetic in the laboratory frame. The transformation rule for  $\gamma$  from the laboratory to the beam frame,  $\gamma' = \gamma_{0\parallel} \gamma (1 - v_{0\parallel} v_{\parallel}/c^2)$ , shows that the particles are not monoenergetic in the beam frame. In the beam frame we find that :

$$\gamma'_{\perp} = \gamma'_{0\perp} + \Delta\gamma'_{\perp}, \quad (28)$$

where

$$\gamma'_{0\perp} = \gamma_0/\gamma_{0\parallel} \quad \text{and} \quad \Delta\gamma'_{\perp} = \gamma_{0\parallel} \gamma_0 (v_{0\parallel} v_{0\perp}/c^2) \Delta\theta.$$

Substituting  $\Delta\gamma'_{\perp}$  into eq. (24) gives a condition on the magnitude of the maximum angular spread,

$$|\Delta\theta|_{\max} \ll \frac{2(\gamma_0 - 1)}{\gamma_0} \frac{\eta}{\gamma_{0\parallel}^2 v_{0\parallel} v_{0\perp}/c^2}, \quad (29)$$

allowed in the cold beam approximation. We will return to conditions (26) and (29) in the next section.

One of the causes of energy spread in an unneutralized beam is the self electrostatic field. For the planar beam that we have considered, the total spread in  $\gamma'_{\perp}$  can be shown to be :

$$\delta\gamma'_{\perp, \text{self}} \approx (\mu') \beta'_{0\perp} ((\Omega_0/\gamma'_{0\perp})/ck_n) \gamma'_{0\perp}, \quad (30)$$

where

$$\mu' = \omega'_b/(\gamma'_{0\perp} \omega'_0) \quad \text{and} \quad \omega'_0 = \Omega_0/\gamma'_{0\perp}.$$

Considering eq. (19), this imposes an upper limit on  $\mu'$ , and hence the beam current in the laboratory frame.

**6. Saturation Mechanism.** — In this section some qualitative arguments concerning the saturation of the electron cyclotron maser instability are presented. There are two mechanisms which are responsible for saturation of the unstable wave in the maser instability. There are i) depletion of the rotational free energy of the electrons and ii) phase trapping of the gyrating particles in the wave. Which of the two mechanisms is actually responsible for saturation in a particular situation depends on the initial beam parameters.

*Case (i) Free Energy Depletion.* — As mentioned in Section 3, the linear dispersion relation, eq. (1), gives rise to a threshold condition for instability given by  $\beta_{0\perp} > \beta_{\perp, \text{crit}}$ . That is, the maximum free energy per particle available to the wave is

$$\varepsilon_{\text{free}} = (\gamma_{0\perp} - \gamma_{\perp, \text{crit}}) m_0 c^2, \quad (31)$$

where

$$\gamma_{\perp, \text{crit}} = (1 - \beta_{\perp, \text{crit}}^2)^{-1/2}.$$

If the beam particles were to lose all of the free energy given by (32), the energy conversion efficiency would be

$$\eta = \frac{\langle \Delta\gamma \rangle}{(\gamma_{0\perp} - 1)} = \frac{(\gamma_{0\perp} - \gamma_{\perp, \text{crit}})}{(\gamma_{0\perp} - 1)} \quad (32)$$

where  $\langle \Delta\gamma \rangle = \gamma_{0\perp} - \gamma_{\perp, \text{crit}}$  is the average change in gamma at saturation and  $\gamma_{0\perp} \gtrsim \gamma_{\perp, \text{crit}}$ . This, of course, is a rough approximation, since as the instability develops the particles warm up, while the threshold condition was obtained for a cold beam. Furthermore, as will be seen, competing processes such as electron trapping may take place before the beam loses its free energy. However, if  $\gamma_{0\perp}$  is slightly greater than  $\gamma_{\perp, \text{crit}}$ , the expression in eq. (31) will represent a good approximation to the actual conversion efficiency. Since, if  $\gamma_{0\perp} \gtrsim \gamma_{\perp, \text{crit}}$ , the particles lose all their free energy before thermalizing or trapping takes place and the wave will be linearly stabilized. If, however,  $\gamma_{0\perp} \gg \gamma_{\perp, \text{crit}}$ , the particles will phase trap in the wave and saturation will occur before all the free energy is used up.

*Case (ii) Phase Trapping.* — The condition for wave saturation due to phase trapping can be viewed in a number of ways. First, we have noted in Section 2 and 3 that the frequency of the wave must be slightly greater than the relativistic electron cyclotron frequency,  $\Omega_0/\gamma_{0\perp}$ , for an instability to develop. Therefore, initially we have

$$\omega - \Omega_0/\gamma_{0\perp} = \Delta\omega \gtrsim 0, \quad (33)$$

where  $\Delta\omega$  is the frequency shift which can be obtained from the linear dispersion relation. Now, as the instability develops the average gamma of the particles,  $\langle \gamma_{\perp} \rangle$ , decreases until  $\omega - \Omega_0/\langle \gamma_{\perp} \rangle = -\Delta\omega$ . At saturation  $\langle \gamma_{\perp} \rangle$  is minimum and :

$$\omega - \Omega_0/\langle \gamma_{\perp} \rangle_s = -\Delta\omega \quad (34)$$

where  $\langle \gamma_{\perp} \rangle_s$  is the average value of  $\gamma_{\perp}$  at saturation. Comparing (33) with (34), we find that at saturation the average change in the gamma of the particles,

$$\langle \Delta\gamma_{\perp} \rangle_s = \gamma_{0\perp} - \langle \gamma_{\perp} \rangle_s,$$

is given by :

$$\langle \Delta\gamma_{\perp} \rangle_s = 2 \gamma_{0\perp} \Delta\omega/\omega. \quad (35)$$

The efficiency of conversion of kinetic energy to field energy,  $\eta$ , when electron phase trapping is responsible for saturation, is :

$$\eta = 2 (\Delta\omega/\omega) \gamma_{0\perp}/(\gamma_{0\perp} - 1). \quad (36)$$

It should be noted that the efficiency in the beam frame cannot be made arbitrarily close to 100 percent simply by increasing the frequency shift,  $\Delta\omega$ . The growth rate of the field is a function of  $\Delta\omega$  and is nonvanishing for a limited range of  $\Delta\omega$ . The relations in (35) and (36) are valid only if  $\Delta\omega$  lies within the nonvanishing part of the growth rate spectrum. To find the actual amplitude of the field at saturation,  $E_{0,s}$ , we use the expression for conservation of total energy given in eq. (18). The maximum field amplitude at saturation is easily shown to be :

$$E_{0,s} = 4 \frac{m_0 c}{|e|} \omega_b (\gamma_{0\perp} \Delta\omega/\omega_0)^{1/2}, \quad (37)$$

where it has been assumed that  $\dot{\alpha}/\omega_0 \ll 1$  and  $ck_n/\omega_0 \approx 1$ .

*Constant of Motion.* — We now examine the nonlinear behavior of the particles with the aid of a constant of the motion derived from the orbit equations.

The orbit equations given in eq. (15) can be written, in the small Larmor radius approximation,  $x \ll a$ , as :

$$\frac{du_{\perp}}{dt} = \frac{|e| E_0}{m_0 c} \cos((\omega_0 + \Delta\omega)t) \times \sin(\varphi(t) + \varphi_0) \quad (38a)$$

$$\frac{d\varphi}{dt} = \frac{\Omega_0}{\gamma_{\perp}} - \frac{|e| E_0}{u_{\perp} m_0 c} \cos((\omega_0 + \Delta\omega)t) \times \cos(\varphi(t) + \varphi_0) \quad (38b)$$

where  $u_{\perp} = \gamma_{\perp} \beta_{\perp}$  is proportional to the transverse particle momentum, and

$$\gamma_{\perp} = (1 + u_{\perp}^2)^{1/2}.$$

The field amplitude,  $E_0$ , as well as the frequency,  $\omega_0 + \Delta\omega$ , are considered fixed and  $\omega_0 = \Omega_0/\gamma_{0\perp}$  is the initial electron cyclotron frequency. The particle momentum,  $u_{\perp} m_0 c$ , and time rate of change of the velocity space angle,  $d\varphi/dt$ , consist of fast and slow time scale variations.

The fast time scale variation is associated with the wave frequency or electron cyclotron frequency, while the slow time scale is associated with the frequency shift,  $\Delta\omega$ . The nonlinear behavior is governed predominantly by the slowly varying parts of  $u_{\perp}$  and  $d\varphi/dt$ . Since  $(\omega_0 + \Delta\omega) - d\varphi/dt$  changes slowly the orbit equations in (38) written on the slow time scale become

$$\frac{du_{\perp}}{dt} = \frac{|e| E_0}{2 m_0 c} \sin(\lambda) \quad (39a)$$

$$\frac{d\lambda}{dt} = (\omega_0 + \Delta\omega) - \frac{\Omega_0}{\gamma_{\perp}} + \frac{|e| E_0}{2 m_0 c u_{\perp}} \cos(\lambda) \quad (39b)$$

where  $\lambda = (\omega_0 + \Delta\omega)t - \varphi(t) - \varphi_0$ . These slow time scale orbit equations have the following constant of motion :

$$C = \frac{|e| E_0}{m_0 c} u_{\perp}(t) \cos(\lambda(t)) + (\omega_0 + \Delta\omega) \times \left( \gamma_{\perp}(t) - \frac{\gamma_{0\perp} \omega_0}{\omega_0 + \Delta\omega} \right)^2. \quad (40)$$

Each particle moves in phase space,  $(u_{\perp}, \lambda)$ , on  $C = \text{constant}$  curves. These  $C = \text{constant}$  curves describe the particle orbits when a constant frequency and constant amplitude field is instantaneously switched on. This situation can be realized by injecting particles into a field filled cavity. The particle trajectories in phase space lie on the constant  $C$  curves depicted in figure 7. The initial conditions for the example

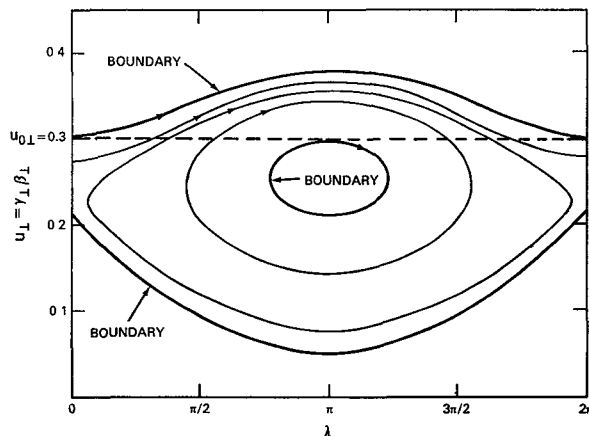


FIG. 7. — Particle trajectories in velocity phase space as found from the constant of the motion. The figure shows the boundaries of the regions accessible to particles initially uniformly distributed between  $0 \leq \lambda \leq 2\pi$  with  $u_{\perp} = u_{0\perp}$ .

shown in the figure 7 are  $\gamma_{0\perp} = 1.05$ ,  $\mu = 0.05$ ,  $\Delta\omega/\omega_0 = 0.018$  and  $|e| E_0/(\gamma_{0\perp} \omega_0 m_0 c) = 0.0025$ . In this illustration the frequency shift is consistent with linear theory and the field amplitude,  $E_0$ , corresponds to roughly a quarter of the value at saturation.

In figure 7 the particles are initially uniformly distributed between  $0 \leq \lambda \leq 2\pi$  with  $u_{\perp} = u_{0\perp}$ . The trajectory followed by a particle is determined by its particular value of  $C$  which is different for each particle. The particles have access to a limited region of phase space, the boundaries of which are shown in figure 7. Particles which initially lie on closed  $C = \text{constant}$  curves are considered trapped even though  $u_{\perp}$  as a function of  $\lambda$  is single valued. However, as the particles travel along their  $C = \text{constant}$  curve,  $u_{\perp}$  will eventually become a multivalued function of  $\lambda$ . Similarly, for a growing field amplitude particles can be considered trapped if they lie on closed  $C = \text{constant}$  curves, long before  $u_{\perp}$  becomes a multivalued function of  $\lambda$ . The character of the accessible  $C = \text{constant}$  curves is determined, among other things, by the value chosen for  $E_0$ . For sufficiently small values of  $E_0$  the particles will not lie on closed  $C = \text{constant}$  curves and, hence, are not trapped. The value of  $E_0$  for which the first closed  $C = \text{constant}$  curve intersects the  $u_{\perp} = u_{0\perp}$  line determines the field amplitude necessary for the onset of trapping. The separatrix separating the closed and open orbits first intersects the line  $u_{\perp} = u_{0\perp}$  at  $\lambda = \pi$ . As larger values of  $E_0$  are chosen, the inaccessible interior region of phase space will contract and approach the point  $u_{\perp} = u_{0\perp}$  and  $\lambda = \pi$ . At the value of  $E_0$  for which the inaccessible interior region vanishes, the average particle energy ceases to decrease. The value of electric field amplitude necessary for the disappearance of the interior region is

$$E_0 \approx 2 \frac{m_0 c \omega_0}{|e|} u_{0\perp} \frac{\Delta\omega}{\omega_0}. \quad (41)$$

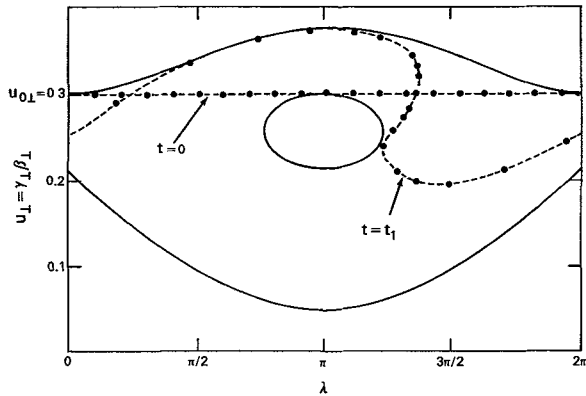


FIG. 8. — The deformation of a monoenergetic beam in the presence of a constant amplitude field showing the actual particle positions in phase space. The curve for  $t = t_0$  indicates the initial positions and the one for  $t = t_1$  the positions when the beam indicates trapping.

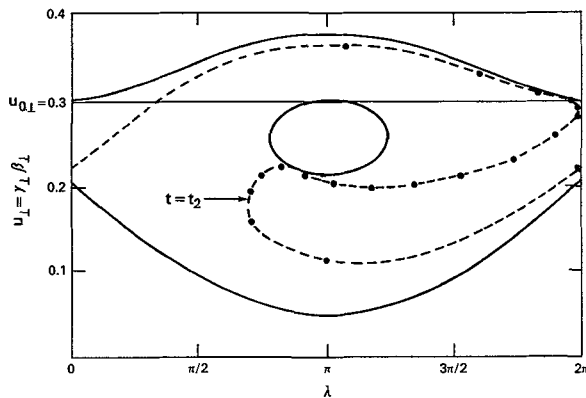


FIG. 9. — The particle positions in phase space for a monoenergetic beam deformed by a constant amplitude electric field at  $t = t_2$  when the particles have lost the maximum energy and are in a state corresponding to saturation.

In figures 8 and 9 the actual positions of the particles in phase space are shown at various times. The parameters used for these figures are the same as those used in figure 7. Superimposed on the curves in figures 8 and 9 are the boundaries of the accessible region of the  $C = \text{constant}$  curves. At  $t = 0$ , when the electric field is switched on, the particles are uniformly distributed along the  $u_{\perp} = u_{0\perp}$  line between  $0 \leq \lambda \leq 2\pi$ . In the constant amplitude electric field the particles proceed to bunch and rotate about the interior boundary as shown in the figures. At  $t = t_1$  the particles begin to overtake each other and bunch along the righthand side of the interior boundary. At a still later time,  $t = t_2$ , the particles rotate and bunch along the bottom of the interior region. At this point the configuration corresponds to the saturation state since the average particle energy is at a minimum. The average kinetic energy continues to oscillate as the particles rotate about the interior boundary in a clockwise direction. The distribution functions,  $f_e(u_{\perp})$ , corresponding to the

phase space trajectories in figures 8 and 9 are shown in figure 10. As can be seen from Figures not all the particles are located at the bottom of the interior boundary at saturation. Consequently, the average of  $u_{\perp}$  at saturation is not exactly given by  $u_{\perp}$  at the bottom of the interior region.

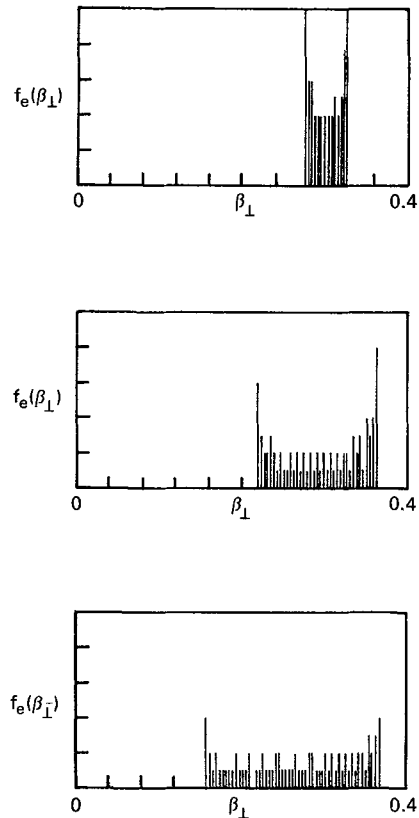


FIG. 10. — The distribution functions of the electron beam deformed by a constant amplitude electric field at  $t = t_0, t_1, t_2$ .

For sufficiently small values of  $E_0$  the accessible  $C = \text{constant}$  curves are open and particles are not trapped. As  $E_0$  is increased, the first particle to become trapped is always the one initially located at  $(u_{0\perp}, \pi)$ . Trapping begins when the particle at  $(u_{0\perp}, \pi)$  has a closed orbit with turning points at  $\lambda = 2\pi$  and  $0$ . At these turning points,  $d\lambda/dt$  vanishes. Since the constant  $C$  is invariant along this closed orbit and  $d\lambda/dt$  vanishes at  $\lambda = 2\pi$  and  $0$ , we can obtain the threshold value of  $E_0$  for trapping from eqs. (39b) and (40). The approximate value of the field amplitude for the onset of trapping is given by :

$$E_0 = \frac{\omega_0 m_0 c}{4 |e| u_{0\perp}} \gamma_{0\perp}^2 \left( \frac{\Delta\omega}{\omega_0} \right). \quad (42)$$

Using the constant of the motion in eq. (40), the minimum value of  $u_{\perp}$  reached by the first trapped particle occurs at  $\lambda = \pi$  and is approximately :

$$u_{\perp, \min} = u_{0\perp} - \frac{2 \gamma_{0\perp}^2}{u_{0\perp}} \left( \frac{\Delta\omega}{\omega_0} \right). \quad (43)$$

The corresponding minimum gamma for this particle is  $\gamma_{\perp, \min} = \gamma_{0\perp} - 2\gamma_{0\perp} \Delta\omega_0/\omega_0$ . Consequently, the first trapped particle undergoes a change in gamma at  $\lambda = \pi$  given by :

$$\Delta\gamma_{\perp} = 2\gamma_{0\perp} \Delta\omega_0/\omega_0. \quad (44)$$

This expression for the maximum change in gamma allows us to estimate the field amplitude at saturation as was done in eq. (37). The change in gamma in eq. (44) is identical to the value found in eq. (35), where a different line of reasoning was used.

**7. Results.** — The nonlinear coupled equations (12) and (15) are solved numerically for a wide range of parameters. In each case the distribution function was represented by approximately 40 to 100 test particles. The actual number of particles used was determined by performing runs with larger and larger numbers of particles until no discernible difference appeared in the results. The conservation of both total system energy and canonical  $y$ -momentum was monitored. The integration timesteps were adjusted to maintain the conservation of both constants to within 0.5 % over the duration of a run. As diagnostic aids, plots of the test particle velocity distribution function, velocity space and phase space were made at various times during the runs.

A run was initiated by uniformly distributing the particles in the velocity space angle,  $0 \leq \varphi_0 \leq 2\pi$  and assigning them the same perpendicular velocity,  $v_{\perp} = v_{0\perp}$ . A small amplitude electric field was introduced as a perturbation and allowed to grow self consistently. From the results of the single wave simulation runs we have made composite graphs of the transfer efficiency from particle kinetic energy to wave electromagnetic energy at saturation as a function of several parameters. A comparison between these results and the analytic predictions in Section 6 shows good qualitative agreement.

We will now discuss the phase space dynamics for the two saturation mechanisms discussed in Section 6. The evolution of the particles in phase space and their distribution functions is shown when saturation occurs by (i) free energy depletion and (ii) phase trapping. In the free energy depletion case the initial parameters are

$$\gamma_{0\perp} = 1.012 \gtrsim \gamma_{\perp, \text{crit}} = 1.0108, \quad \mu = 0.05,$$

where  $\mu$  is a dimensionless parameter related to the beam density through

$$\mu = \omega_b / (\sqrt{\gamma_{0\perp}} \omega_0), \quad \omega_0 = ck_n = l\Omega_0/\gamma_{0\perp}$$

and  $l = n = 1$ . Figures 11a and 11b show the particle phase space in the course of the instability when the growth is still linear. At saturation, shown in figure 11c, the particles indicate no phase trapping. The average particle  $\gamma_{\perp}$  at saturation is within a few percent of  $\gamma_{\perp, \text{crit}}$ . However, the individual particles energies

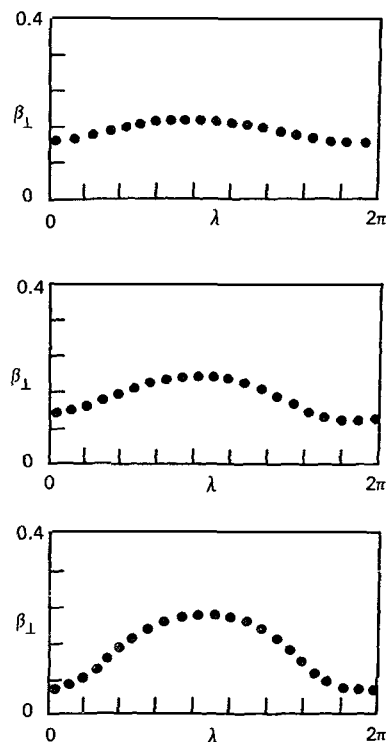


FIG. 11. — The particle positions in phase space from a simulation of the cyclotron maser instability in the case of saturation by energy depletion, (a)  $t = t_1$  linear phase, (b)  $t = t_2$  nonlinear phase, and (c)  $t = t_3$  at saturation.

have a large variation, as can be seen from the distribution functions depicted in figures 12b and 12c. The predicted efficiency according to eq. (32) is  $\eta = (\gamma_{0\perp} - \gamma_{\perp, \text{crit}})/(\gamma_{0\perp} - 1) \approx 10\%$ . This is in excellent agreement with the numerically evaluated efficiency of 10%. To illustrate case (ii), where phase space trapping is responsible for saturation, we choose the parameters  $\gamma_{0\perp} = 1.2$ ,  $\mu = 0.05$ . (Note that  $\gamma_{\perp, \text{crit}} = 1.01$  for this case as in case (i).) The particle dynamics in velocity phase space and the velocity distribution function are shown at various times  $\tau$  during the evolution of the run in figures 13 and 14. In figure 13a the particles are shown at  $\tau = 250$  when they have begun to display some bunching but are relatively close to their initial phase space positions. The corresponding distribution function in figure 14a displays little spread in velocity. When the nonlinear effects manifest themselves by a change in the growth rate, the velocity phase space bunching becomes distinctly visible and the velocity distribution begins to spread as shown in figures 13b and 14b. In figures 13c and 14c we show the velocity phase space and distribution function at saturation. The phase space plots in figures 13b and 13c show the trapped electrons circulating and forming a tongue configuration, similar to the one in figures 8 and 9, where a constant electric field was present. The saturation mechanism for this case is clearly phase trapping of the beam electrons in the wave. Because not

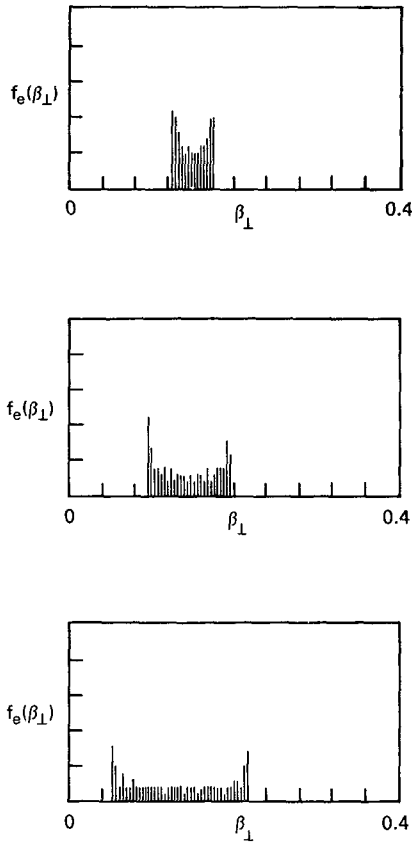


FIG. 12. — The distribution function of the electrons from a case of saturation by energy depletion at various times as in Figure 10.

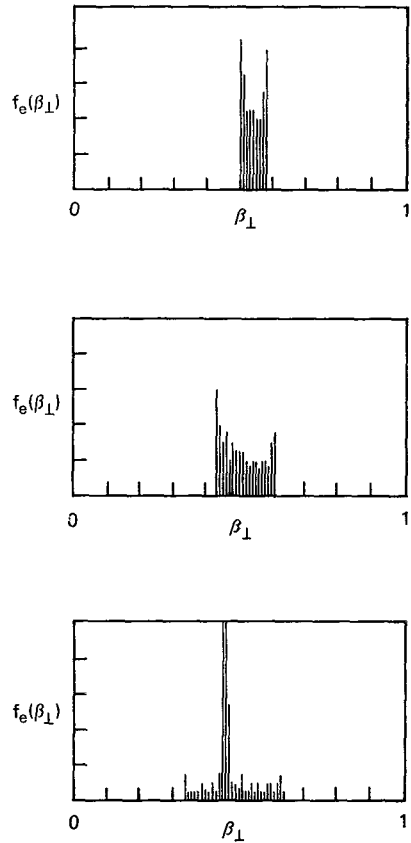


FIG. 14. — The distribution function for saturation by trapping for times given in figure 12.

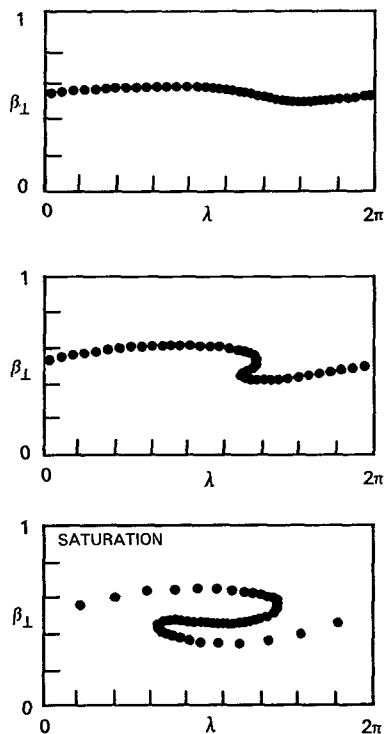


FIG. 13. — Particle positions in phase space from a simulation in the case of saturation by trapping, (a) linear phase, (b) non-linear phase, and (c) at saturation.

all the electrons are trapped, an average over the distribution function is necessary to determine  $\langle \gamma_{\perp} \rangle_s$ . This necessitates the introduction of a numerical factor,  $f$  in the simple expression corresponding to eq. (35)

$$\langle \Delta \gamma_{\perp} \rangle_s / \gamma_{0\perp} = 2 f \Delta \omega / \omega_0 .$$

The factor  $f$  is a number on the order of unity and depends on the fraction of deeply trapped particles,  $f \lesssim 1$ .

As an example of a typical run, we shall follow the evolution of field and particle quantities as a function of time. The initial conditions chosen for this example are :

$\mu = 0.05$ ,  $\gamma_{0\perp} = 1.05$ ,  $\omega_0 = ck_n = \Omega_0 / \gamma_{0\perp}$  and  $n = 1$ , and  $\mu = \omega_h / (\sqrt{\gamma_{0\perp}} \omega_0)$ . In figure 15, the nonlinear frequency shift and growth rate are shown as functions of the normalized time parameter  $\tau = \omega_0 t$ . Initially for  $\tau \lesssim 150$  when the field amplitude is small, we see a transient, during which the perturbing field comes into equilibrium with the particles. That is, initially the presence of the small amplitude electric field is inconsistent with the initial conditions of the beam particles. During the early transient the field and particles adjust themselves to self consistently satisfy eqs. (12) and (15). The transient regime lasts for a time roughly given by

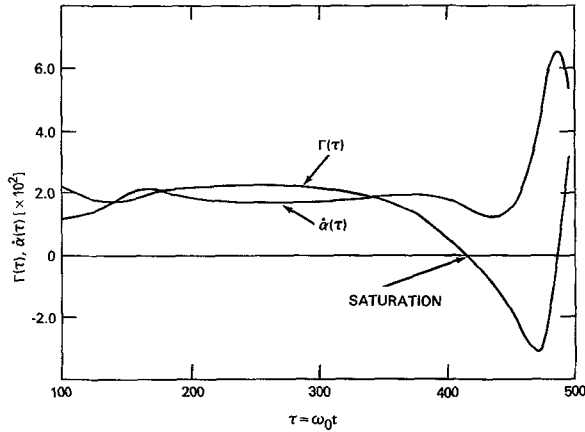


FIG. 15. — The nonlinear phase shift and growth rate as a function of time for a typical simulation.

$\tau_{\text{tran}} \approx \omega_0/\Gamma_L$ . The linear regime,  $150 \lesssim \tau \lesssim 350$ , follows the initial transient. In this regime the wave grows exponentially and both the growth rate and frequency shift assume the values predicted by linear theory. As will be apparent from one of our later figures, the growth rates and frequency shifts in the linear regime are in excellent agreement with those found from the linear dispersion relation. The exponentially growing wave attains a sufficiently high amplitude by  $\tau = 350$  to start nonlinearly affecting the particle dynamics and the growth rate begins to decrease until it reaches zero at  $\tau \approx 420$  when saturation occurs.

The nonlinear change in the growth rate is accompanied by a less pronounced change in the frequency shift prior to saturation. We find that for the parameters used in this example at saturation

$$\omega_0 + \dot{\alpha}(\tau) - \Omega_0 / \langle \gamma_{\perp} \rangle \approx 0$$

in good agreement with the qualitative argument in Section 6. The normalized field amplitude,

$$\varepsilon_0(\tau) = |e| E_0(\tau) / (m_0 c \omega_0),$$

and the average perpendicular particle energy  $\langle \gamma_{\perp} \rangle$  are shown as functions of  $\tau$  in figure 16.

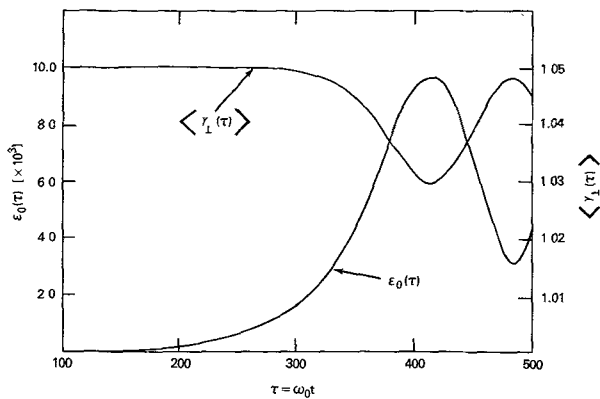


FIG. 16. — The field amplitude and average beam  $\gamma$  as a function of time for a typical simulation.

We have found that the energy efficiency curves for a given set of parameters always display a maximum. For example, with  $\mu = 0.1$ , the efficiency curve shown in figure 16 has a peak of 40 % when  $\gamma_{0\perp} = 1.1$ . The peak results from the competition between the two saturation mechanisms described in Section 6. As can be seen in figure 17 the efficiency curve has a cutoff at  $\gamma_{\perp} = \gamma_{\perp, \text{crit}} = 1.0185$ . The curves of the linear growth rates and frequency shifts, obtained by numerically solving the linear dispersion relation of eq. (1) are shown in figure 18 as a function of  $\gamma_{0\perp}$ . The linear growth rate curve shows a threshold

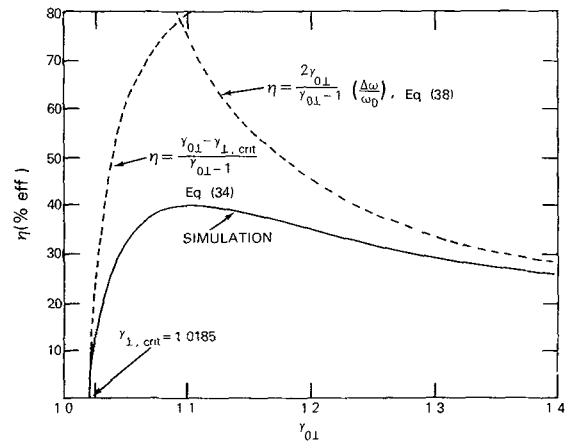


FIG. 17. — The efficiency of the cyclotron maser as a function of energy found from the two mechanisms of saturation and from simulations.

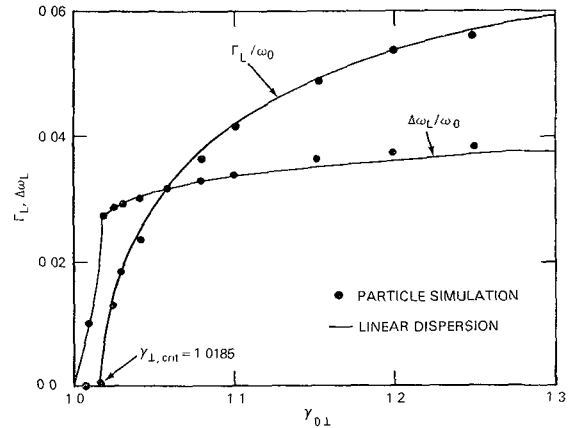


FIG. 18. — A comparison of the growth rate and phase shift predicted by linear theory and the results from the linear portions of the computer simulations.

at  $\gamma_{0\perp} = 1.0185$ , identical to that in figure 18. Figure 18 also shows a comparison between the results of linear theory, eq. (1), and of the particle simulations in the linear regime. Clearly, the linear growth rates and frequency shifts are in excellent agreement. For beams that have initial energies characterized by  $\gamma_{0\perp} \gtrsim \gamma_{\perp, \text{crit}}$ , we find that the excited wave extracts free energy from the beam until  $\langle \gamma_{\perp} \rangle = \gamma_{\perp, \text{crit}}$

and the system becomes linearly stable without particle trapping taking place. The simulations confirm this, since the velocity phase space plots show no evidence of trapping at the time of saturation when  $\gamma_{0\perp} \gtrsim \gamma_{\perp, \text{crit}}$ . In this regime a rough expression for the average change in  $\gamma_{\perp}$  at saturation is

$$\langle \Delta\gamma_{\perp} \rangle_s = \gamma_{0\perp} - \gamma_{\perp, \text{crit}}$$

and implies an efficiency monotonically increasing with  $\gamma_{0\perp}$ ; this is shown as a dashed curve on figure 17. In the other regime where  $\gamma_{0\perp} \gg \gamma_{\perp, \text{crit}}$  the saturation mechanism is dominated by particle trapping and we find that  $\langle \Delta\gamma_{\perp} \rangle_s = 2f\gamma_{0\perp} \Delta\omega/\omega_0$ . This implies an efficiency curve monotonically decreasing with  $\gamma_{0\perp}$  as shown in figure 17 with  $f = 1$ . The two saturation mechanisms described here predict an efficiency maximum: this is also verified by the results of the particle simulations.

Our saturation arguments show qualitative agreement with the actual efficiency obtained numerically. In the  $\gamma_{0\perp} \gg \gamma_{\perp, \text{crit}}$  regime we have arbitrarily set  $f = 1$ , implying that all the particles are deeply trapped at saturation. From figure 17 we see that in the intermediate regime  $f$  is closer to  $1/2$ . Similar arguments hold in the  $\gamma_{0\perp} \gtrsim \gamma_{\perp, \text{crit}}$  regime. The dashed curves in figure 17 show the competition between two mechanisms leading to a maximum in the efficiency curves.

We now present the results of our nonlinear analysis for a wide range of parameters. In figure 19, energy efficiency as a function of  $\gamma_{0\perp}$  is shown for various values of  $\mu$ ,  $\mu = 0.025, 0.05, 0.15$  and  $0.35$ .

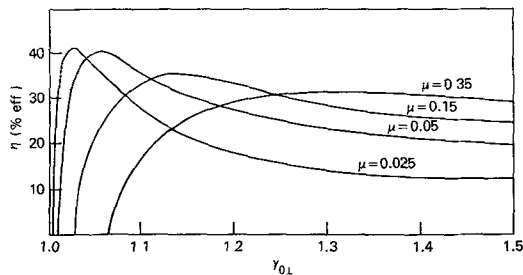


FIG. 19. — The beam frame efficiency of the electron cyclotron maser as a function of energy for various densities when  $ck_n = \Omega_0/\gamma_{0\perp}$ .

In this figure the initial wave frequency  $\omega_0$  was set equal to  $ck_n$  with  $n = 1$ . Furthermore, the initial relativistic cyclotron frequency,  $\Omega_0/\gamma_{0\perp}$  was set equal to  $ck_n$ . These initial conditions on  $\omega_0$ ,  $ck_n$  and  $\Omega_0/\gamma_{0\perp}$  were selected because they occur near the maximum linear growth rate. All of the curves in figure 19 display a maximum in efficiency in the beam frame as a function  $\gamma_{0\perp}$ . This characteristic of the curves has already been explained. A further feature of the curves is that as  $\mu$  increases,  $\gamma_{0, \text{crit}}$  increases in agreement with the definition of  $\beta_{\perp, \text{crit}}$  given in Section 3. From figure 19 we also note that the efficiency in-

creases at low values of  $\gamma_{0\perp}$  as  $\mu$  is decreased. This property of the curves can be explained by noting that as  $\mu$  decreases,  $\gamma_{\perp, \text{crit}}$  decreases, resulting in a sharp increase in efficiency as a function of  $\gamma_{0\perp}$  near  $\gamma_{\perp, \text{crit}}$ . The maximum efficiency seems to level off at  $\sim 40\%$  for low values of  $\gamma_{0\perp}$ , when

$$\omega_0 = ck_n = \Omega_0/\gamma_{0\perp}.$$

Dramatic increases in the efficiency can be realized in a number of ways. For example, by slightly mistuning the relativistic cyclotron frequency away from  $\omega_0 = ck_n$ , electron phase trapping can be postponed and higher efficiencies realized. In the regime where electron trapping is responsible for saturation, we have shown that the efficiency is roughly

$$2f\gamma_{0\perp}(\omega_0 + \Delta\omega - \Omega_0/\gamma_{0\perp})/(\gamma_{0\perp} - 1).$$

By choosing  $\omega_0 > \Omega_0/\gamma_{0\perp}$ , we can expect the efficiency to increase. In figure 20 the efficiency is shown as a function of  $(\Omega_0/\gamma_{0\perp})/\omega_0$  for various values of  $\mu$  and  $\gamma_{0\perp}$ . The values for  $\mu$  and  $\gamma_{0\perp}$  were taken from the maximum efficiency points in figure 19. Figure 20 shows clearly that higher efficiencies can be realized for  $(\Omega_0/\gamma_{0\perp})/\omega_0$  less than unity. Since sufficiently

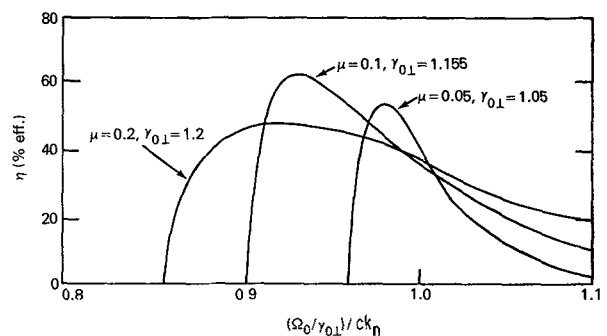


FIG. 20. — The beam frame efficiency of the electron cyclotron maser when the cyclotron frequency is varied.

small values of  $(\Omega_0/\gamma_{0\perp})/\omega_0$  lie outside the growth rate spectrum, the efficiency drops to zero. By mistuning the magnetic field, the efficiency was increased from 40% to 63% in the beam frame for the case  $\mu = 0.1$  and  $\gamma_{0\perp} = 1.155$ .

The efficiency can also be increased by varying the external magnetic field in time in such a way that  $\omega - \Omega_0(\tau) / \langle \gamma_{\perp}(\tau) \rangle$  is held fixed. This procedure is similar to the mistuning approach discussed, in that electron phase trapping is postponed. Choosing  $\mu = 0.1$ ,  $\gamma_{0\perp} = 1.1$  and changing the magnetic field in time such that  $(\omega - \Omega_0(\tau) / \langle \gamma_{\perp}(\tau) \rangle)$  is fixed at its initial value of 0.034, an efficiency of  $\approx 70\%$  was realized. This compares with an efficiency of  $\approx 40\%$  when the magnetic field was held fixed at  $\Omega_0/\gamma_{0\perp} = \omega_0 = ck_n$ .

**8. Experimental Examples.** — The theory presented above is most directly applicable to a gyrotron in

the form of a travelling wave amplifier (gyro-TWT). In such an amplifier the drift tube containing the magnetized, spiralling, electron beam serves as a simple r. f. structure (a waveguide) into which an e. m. wave may be introduced. To optimize energy transfer from the beam to the wave both group velocity and phase velocity of the wave are nearly matched to the group and phase velocity of the beam fast cyclotron wave. This is equivalent to having the wave frequency nearly equal to both the mode cutoff frequency and to the electron cyclotron frequency in the beam frame ( $v'_{0\parallel} = 0$ ).

A linear gyro-TWT amplifier was first realized [27] by launching a  $TE_{01}$  wave into a cylindrical drift tube containing an intense relativistic electron beam. The amplifier was operated in the linear regime exhibiting a power gain of 16 dB (1 dB/cm) for a total power output of 4 MW at 8.6 GHz. The observed gain agreed well with the predictions of the linear theory as did other features of the experimental data such as resonant magnetic field and width of the magnetic resonance. The amplifier had a bandwidth of  $\sim 5\%$  and appeared to be magnetically tunable over a very wide range in frequency ( $\sim$  octave). However, the nonlinear operation of the amplifier was not examined because the power of the input source ( $\sim 100$  kW) was so much smaller than the beam power ( $\sim 5$  GW).

The nonlinear theory has recently been applied [28] to the detailed design of a highly efficient saturated gyro-TWT amplifier working with an electron beam of more modest power level. To improve the accuracy of the calculation, the theory was adapted to cylindrical geometry. Rather than using an intense relativistic electron beam generator with its short single pulse operation ( $\tau \sim 50$  ns), it was decided to use a magnetron injection gun with thermionic cathode such as used in the gyrotron experiments at the Gorkii State University [11, 12]. Such a choice makes

long pulse operation possible, and opens the way for application of the device to r. f. heating of plasmas.

As in the linear intense beam experiment, an operation of the nonlinear amplifier was chosen to be in the  $TE_{01}$  mode and at the fundamental electron cyclotron frequency. Power output of the gyrotron was chosen to be several hundred kilowatts at  $f \approx 35$  GHz to match the parameters of an easily accessible research Tokamak [29] on which electron

TABLE I

*Design Parameters of Optimized Gyro TWT*

A. Lab Frame Parameters

- $\omega_0/2\pi = 35$  GHz
- $V = 71$  kV
- $I = 9.5$  A
- $\eta = 51\%$
- $P_0 = \eta VI = 340$  kW
- $v_{0\perp}/v_{0\parallel} = 1.5$
- $B_0 = 12.9$  kG
- drift tube radius  $r_g = 5.37$  mm
- beam guiding center radius  $r_b = 2.52$  mm\*
- linear power gain = 2.0 dB/cm

B. Beam Frame Parameters

- $\gamma'_{0\perp} = 1.10$
- $\mu' = \frac{4\pi e^2 \sigma'_0}{m_0 r_g \gamma'_{0\perp} ck_n} = 0.023$
- $\eta' = 70\%$
- $(\Omega_0/\gamma'_{0\perp})/ck_n = 0.96$

(\*)  $r_b$  was chosen to correspond to radius of  $E$  field maximum in  $TE_{01}$  mode.

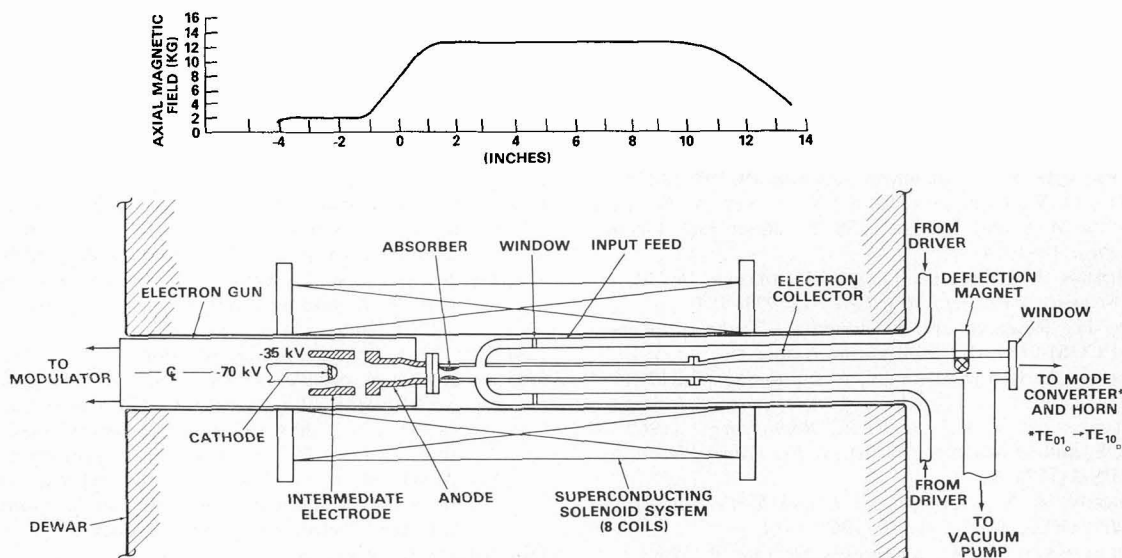


FIG. 21. — Schematic of Gyro-Travelling Wave Amplifier.

cyclotron resonance heating (ECRH) experiment will be carried out.

In order to proceed with a design optimized for maximum efficiency, one needs to specify the velocity ratio  $v_{0\perp}/v_{0\parallel}$  in addition to the output power,  $P_0$ , and frequency,  $\omega_0$ . A large value of  $v_{0\perp}/v_{0\parallel}$  would seem desirable since only the transverse component of energy is converted to e. m. radiation in the cyclotron maser instability. However, if  $v_{0\perp}/v_{0\parallel}$  is too large an excessive build-up of space charge would result and complicate the operation of the amplifier. We have chosen  $v_{0\perp}/v_{0\parallel} = 1.5$ .

Having chosen  $v_{0\perp}/v_{0\parallel}$  and  $\omega_0$ , beam frame parameters such as  $\mu'$ ,  $\gamma'_{0\perp}$ , and  $\eta'$  can be related to current, voltage and efficiency in the laboratory frame. Then using sets of beam-frame characteristics curves such as those in figures 19 and 20, parameters can be determined which maximize efficiency at the desired value of output power.

An optimized set of parameters for the desired 35 GHz gyro-TWT is presented in table I. The amplifier is sketched in figure 21. The configuration of

electrodes in the gun the applied voltages and the magnetic field contour were chosen to yield the design values of  $I$ ,  $r_b$ , and  $v_{0\perp}/v_{0\parallel}$  while minimizing the velocity spread. A numerical gun simulation, including space charge effects, traced electron trajectories, and determined that for the gun design shown in figure 21, the spread in transverse velocity is 3.5 % while the spread in streaming velocity is 6.8 %. The spread in energy was 0.2 %. These values are sufficiently small to strongly satisfy the energy spread condition derived above in Section 5.

The gyro-TWT shown in figure 21 is presently being fabricated along with a gyromonotron single cavity oscillator which will use the same electron gun and solenoid system. It is hoped to employ these gyrotrons in ECRH studies within the year.

**Acknowledgments.** — S. Kulpa of the Harry Diamond Laboratory assembled the data presented in figure 1. Great assistance was derived from discussions with C. K. Chu, W. M. Manheimer, E. Ott, M. Read and L. Seftor.

#### References

- [1] TWISS, R. Q., *Austr. J. Phys.* **11** (1958) 564.
- [2] SCHNEIDER, J., *Phys. Rev. Lett.* **2** (1959) 505.
- [3] GAPANOV, A. V., *Izv. VUZ., Radiofizika* **2** (1959) 450, and *Kzv. VUZ., Radiofizika* **2** (1959) 836.
- [4] PANTELL, R. H., *Proc. IRE* **47** (1959) 1146.
- [5] HIRSHFIELD, J. L. and WACHTEL, J. M., *Phys. Rev. Lett.* **12** (1964) 533.
- [6] FLYAGIN, V. A., GAPANOV, A. V. PETELIN, M. I. and YULPATOV, V. R., *IEEE Trans. MTT-25* (1977) 514; HIRSHFIELD, J. L. and GRANATSTEIN, V. L., *IEEE Trans. MTT-25* (1977) 522.
- [7] GRANATSTEIN, V. L., HERNDON, M., SPRANGLE, P., Y. CARMEL and NATION, J. A., *Plasma Phys.* **17** (1975) 23.
- [8] GRANATSTEIN, V. L., HERNDON, M., PARKER, R. K. and SCHLESINGER, S. P., *IEEE Trans. MTT-22* (1974) 1000.
- [9] FRIEDMAN M. and HERNDON, M., *Phys. Fluids* **16** (1973) 1982.
- [10] ALIKAEV, V. V., BOBROVSKII, G. A., POZNYAK, V. I., RAZUMOVA, K. A., SANNIKOV, V. V., SOKOLOV, YU. A., and SHMARIN, A. A., *Sov. J. Plasma Phys.* **2** (1976) 212.
- [11] ZAYTSEV, N. I., PANKRATOVA, T. B., PETELIN, M. I. and FLYAGIN, V. A., *Radiotekh. Electron.* **19** (1974) 1056.
- [12] DISEL', D. V., KORABLEV, G. S., NAVEL'YEV, V. G., PETELIN, M. I. and TSIMRING, Sh. E., *Radio Eng. Electron. Phys.* **19** (1974) 95.
- [13] FRIEDMAN, M., HAMMER, D. A., MANHEIMER, W. M. and SPRANGLE, P., *Phys. Rev. Lett.* **31** (1973) 752.
- [14] JORY, H., Research and Development Technical Report, ECOM-01873-F (1968) Varian Associates.
- [15] BRATMAN, V. L. and TOKAREV, A. E., *Radiofizika* **17** (1974) 1224.
- [16] ZHELZNYNSKOV, V. V., *Izv. VUZ., Radiofizika* **3** (1960) 57.
- [17] OTT, E. and MANHEIMER, W. M., *IEEE Trans. Plasma SC., PS-3* (1975) 1.
- [18] GAPANOV, A. V., PETELIN, M. I. and YULPATOV, V. K., *Izv. VUZ., Radiofizika* **10** (1967) 1414.
- [19] ZHURAKOVSKIY, V. A., *Radiotekh. Electron.* **9** (1964) 1527.
- [20] RAPOPORT, G. N., NEMAK, A. K. and SHURAKOVSKIY, V. A., *Radiotekh. Electron.* **12** (1967) 4, 587.
- [21] NUSINOVICH, G. S. and ERM, R. E., *Elektronnaya Tekhnika, Sec. 1, Elektronika SVCH*, No. 22 (1972) 55.
- [22] DEMIDOVICH, E. M., KOVALEV, I. L., KURAYEV, A. A. and SHEVCHENKO, F. C., *Radiotekh. Electron.* **18** (1973) 10, 2097.
- [23] SPRANGLE, P. and MANHEIMER, W. M., *Phys. Fluids* **18** (1975) 224.
- [24] SPRANGLE, P. and DROBOT, A. T., *IEEE Trans. MTT-25* (1977) 528.
- [25] In Ref. [18], a dispersion relation is derived, which is a special case of eq. (1). In this reference, the transverse wave number is assumed to vanish,  $ck_{\perp} = 0$ . It is found that instability can still exist for finite  $k_0$  if
 
$$\beta_{0\perp}^2 > 1 - \beta_{0\parallel}.$$
 The growth rate is given by
 
$$\Gamma = (\omega_0/\sqrt{2}) (1 - \beta_{0\parallel} - \beta_{0\perp}^2)^{1/2}$$
 for  $l = 1$  and  $n = 0$ .
- [26] It should be noted that the righthand side of the expression for  $\beta_{\perp, \text{crit}}$  is also a function of  $\beta_{\perp, \text{crit}}$ . In the given expression for  $\beta_{\perp, \text{crit}}$ ,  $\beta_{\perp}$  should be replaced by  $\beta_{\perp, \text{crit}}$ .
- [27] GRANATSTEIN, V. L., SPRANGLE, P., HERNDON, M., PARKER, R. K. and SCHLESINGER, S. P., *J. Appl. Phys.* **46** (1975) 3800.
- [28] CHU, C. K., private communication.
- [29] According to private conversations with G. BEKEFI, the VERSATOR II tokamak at MIT has ohmic heating power of  $\sim 200$  kW and a magnetic field variable from 4 kG to 15 kG. Thus with a gyrotron at 35 GHz it should be possible to do ECRH experiments at both the fundamental and the 2nd harmonic of the tokamak electron cyclotron frequency.
- [30] SEFTOR, L., private communication.